A Study of Latent Heat of Vaporization

in Aqueous Nanofluids

by

Soochan Lee

A Dissertation Presented in Partial Fulfillment
of the Requirements for the Degree
Doctor of Philosophy

Approved June 2015 by the
Graduate Supervisory Committee:

Patrick E. Phelan, Co-Chair
Carole-Jean Wu, Co-Chair
Robert Wang
Liping Wang
Robert A. Taylor
Ravi Prasher

ARIZONA STATE UNIVERSITY

August 2015

ABSTRACT

Nanoparticle suspensions, popularly termed “nanofluids,” have been extensively investigated for their thermal and radiative properties. Such work has generated great controversy, although it is arguably accepted today that the presence of nanoparticles rarely leads to useful enhancements in either thermal conductivity or convective heat transfer. On the other hand, there are still examples of unanticipated enhancements to some properties, such as the reported specific heat of molten salt-based nanofluids and the critical heat flux. Another largely overlooked example is the apparent effect of nanoparticles on the effective latent heat of vaporization (h_{fg}) of aqueous nanofluids. A previous study focused on molecular dynamics (MD) modeling supplemented with limited experimental data to suggest that h_{fg} increases with increasing nanoparticle concentration.

Here, this research extends that exploratory work in an effort to determine if h_{fg} of aqueous nanofluids can be manipulated, i.e., increased or decreased, by the addition of graphite or silver nanoparticles. Our results to date indicate that h_{fg} can be substantially impacted, by up to ± 30% depending on the type of nanoparticle. Moreover, this dissertation reports further experiments with changing surface area based on volume fraction (0.005% to 2%) and various nanoparticle sizes to investigate the mechanisms for h_{fg} modification in aqueous graphite and silver nanofluids. This research also investigates thermophysical properties, i.e., density and surface tension in aqueous nanofluids to support the experimental results of h_{fg} based on the Clausius - Clapeyron equation. This theoretical investigation agrees well with the experimental results. Furthermore, this research investigates the h_{fg} change of aqueous nanofluids with nanoscale studies in terms of melting of silver nanoparticles and hydrophobic interactions of graphite nanofluid. As a

result, the entropy change due to those mechanisms could be a main cause of the changes of h_{fg} in silver and graphite nanofluids.

Finally, applying the latent heat results of graphite and silver nanofluids to an actual solar thermal system to identify enhanced performance with a Rankine cycle is suggested to show that the tunable latent heat of vaporization in nanofluilds could be beneficial for real-world solar thermal applications with improved efficiency.

ACKNOWLEDGMENTS

First of all, I would like to thank my wife, Hyewon Shin, and my boy, Matthew H. Lee, for supporting me to pursue the PhD. Without their help and love, I could not finish my degree. Second, special thanks to co-chair, Dr. Patrick E. Phelan for giving me an opportunity to start solar thermal research at Arizona State University and offering me valuable comments and ideas to develop my work during my PhD. I would also like to express my gratitude to co-chair, Dr. Carole-Jean Wu for spending valuable time to provide feedback and giving me the constant guidance and support, which have been helpful to improve my research. I would also like to acknowledge the rest of my committee members Dr. Robert Wang, Dr. Liping Wang, Dr. Robert A. Taylor, and Dr. Ravi Prasher for sharing their ideas and advising me throughout this process. Based on all committee members' comments, this work could be possible. I would also like to thank my lab mates, Andrey, Carlos, Nick, Turki, and Sami for giving me their constant support and help to improve my PhD work. Finally, I would like to thank my family, professors, and friends in Korea for giving me their constant support during my PhD and this dissertation has been possible due to so many people, who I may not be able to list here.

TABLE OF CONTENTS

Page

LIST OF TABLES vi

LIST OF FIGURES vii

NOMENCLATURE xii

CHAPTER

1. INTRODUCTION 1

1.1 Nanofluids 2

1.2 Latent Heat of Vaporization in Pure Water 2

1.3 Historical Attempts to Manipulate the Latent Heat 3

1.4 Volumetric Solar Thermal Collector 9

1.5 Motivation 11

1.6 Research Goals 15

2. EXPERIMENTAL INVESTIGATION OF THE LATENT HEAT OF VAPORIZATION IN AQUEOUS NANOFLUIDS 17

2.1 Experimental Setup and Procedure 17

2.2 Experimental Method 23

2.3 Experimental Results and Discussion 28

2.4 Summary 43

3. MEASUREMENT OF THERMOPHYSICAL PROPERTIES FOR LATENT HEAT OF VAPORIZATION IN AQUEOUS SILVER AND GRAPHITE NANOFLUIDS 44

CHAPTER Page

3.1 Clausius-Clapeyron Equation for h_{fg} 44

3.2 Theoretical Results and Discussion 50

4. NANOSCALE STUDIES FOR LATENT HEAT OF VAPORIZATION IN AQUEOUS NANOFLUIDS 53

4.1 Low Temperature Melting of Silver Nanoparticles in Subcooled and Saturated Pure Water 54

4.1.1 Surface Melting of Silver Nanoparticles in Water 56

4.1.2 Hamaker Constant for Surface Melting-Based Aqueous Nanofluid 59

4.1.3 Experimental Approach and Discussion 67

4.1.4 Summary 77

4.2 Hydrophobic Interactions of Graphite Nanoparticles in Saturated Water 78

5. SOLAR THERMAL APPLICATION 81

5.1 Vapor Power Systems - Rankine Cycle 81

5.2 Nanofluid-Based Solar Thermal Collector 82

5.3 Nanofluid-Based Solar Thermal Storage 87

6. CONCLUSIONS AND SUGGESTIONS FOR FUTURE WORK 89

REFERENCES 91

APPENDIX

A Reflectance and Thermal Loss Calculations 97

B Uncertainty Calculation for the Experimantal Results 101

LIST OF TABLES

Table Page

1. Review of Latent Heat of Nanofluids [20] 5
2. Values of Latent Heat of Vaporization in Aqueous Nanofluids 9
3. The Values of All Three Terms on the RHS of Eq. (27), for the Laser Experiment Shown in Fig. 8 (a), Where t_F = 20 min and 0.1% Volume Fraction Nanofluid. 26
4. The Values of All Three Terms on the RHS of Eq. (2), for the Hot Wire Experiment with a Heat Gun Shown in Fig. 8 (b), Where t_F = 20 min and 0.1% Volume Fraction of Nanofluids. 27
5. The Values of All Three Terms on the RHS of Eq. (2), for the Hot Wire Experiment with a Well-Insulated Sample Shown in Fig. 8 (c), Where t_F = 5 min and 0.1% Volume Fraction of Nanofluids (Zero Background Vapor Mass Generation) 28
6. The Results of h_{fg} in Fluids Using a Laser.....29
7. The Results of h_{fg} in Fluids Using a Hot Wire.....30
8. The Results of h_{fg} in Fluids without a Heat Gun.....32
9. The Measured (Averaged) and Extrapolated Surface Tension Results of Fluids.....50
10. The Theoretical Results of h_{fg} in Nanofluids and Pure Water with Surfactant, Based on Eq. (13).....51

Table Page

11. Parameters for the Calculation of the Temperature-Dependent Dielectric Permittivity of Solid and Liquid Silver (Melting Temperature is Calculated Based on the Eq. in Fig. 16. 65

12. Calculated Hamaker Constant Values A132 zJ (zepto Joule, 10^{-21}) at the Melting Temperature of Various-Sized Silver Nanoparticles in Subcooled (25°C) Water. 66

LIST OF FIGURES

Figure Page

1. The Enhancement of h_{fg} of Water as a Function of the Volume Fraction and the Platinum Nanoparticle Size based on Molecular Dynamics (MD) Simulations [7].....4
2. Thermal Resistance Network of a Conventional Solar Thermal Plant and a Nanofluid-Based Volumetric Solar Thermal Plant [15]. 10
3. Schematic of Solar Steam Generation based on Nanoparticles [17] 12
4. Vapor Generation around Graphite Nanoparticles in Water with a Laser Irradiance of 770 W/cm^2. Dashed Circles Indicate Separated High Concentrations of Graphite Nanoparticles [16]. 13
5. Suggested Volumetric Solar Thermal System Using Nanofluids.....14
6. Experimental Setup for Measuring the Latent Heat of Vaporization in Nanofluids with (a) Laser-Based Heating, (b) Hot Wire-Based Heating 18
7. Experimental Setup – Taken Using a Digital Camera 19
8. Schematic Diagram for (a) Laser and a Heat Gun, (b) A Hot Wire and a Heat Gun, (c) a Hot Wire and Well-Insulated Sample, (D) Boiling Experiments Procedure 21
9. Visual Images Exposed to Laser Beam (a) Prepared Nanofluids with Pure Water (b) Bubbles in Test Cells during the Experiments 22
10. (A) Schematic Diagram of the Experimental Set-up for Measuring the Latent Heat of Vaporization in Nanofluids using a Hot Wire with Electrical Source.

Figure Page

(B) Schematic Representation of Well-Insulated Boiling Test Cell to Reduce Heat Loss by Convection and Radiation.....31

11. Vapor Mass Generation based on Laser and a Heat Gun Experiment as a Function of Time for Pure Water with and without Surfactant (SDS), 0.1% by Volume, 20-nm Silver Nanofluid with 1% Surfactant, and 0.1% by Volume, 30-nm Graphite Nanofluid with 1% Surfactant.....33
12. (a) Measured Latent Heat of Vaporization in Graphite Nanofluids and (b) in Silver Nanofluids (the Trends are Changed after 1% Volume Fraction), Including Calculated Latent Heat of Vaporization in Graphite and Silver Nanofluid Using Eq. (1) based on Changes in the Volume Fraction [14].....36
13. Absolute Values of the Increased h_{fg} for Graphite and Aluminum Oxide Nanofluids [7] and the Decreased h_{fg} of Silver Nanofluids relative to that for Pure Water with Surfactant (2132 kJ kg-1) (%) [7] in terms of Surface Area Changes, Compared with Ameen's Results for Aluminum Oxide Nanoparticles [7]. That is, the Relative Change in h_{fg} Increases with Increasing Surface Area. The Trends Change at the Circled Points near 2% Volume Fraction for Silver and Graphite Nanofluids because of Agglomeration.....38
14. Average Size Change of 2% Volume Fraction, 30-nm (a) Graphite Nanofluid before Heating (48 ± 2nm, upper) and (178 ± 2nm, lower) after Heating, and (b) 2% Volume Fraction, 20-nm Silver Nanofluids (27nm ± 2nm, upper) before Heating and after Heating (90nm ± 2nm, lower).....42

Figure Page

15. The Surface Tension Changes in Nanofluids with 1% Surfactant as a Function of the Temperature (a) the Measured Surface Tension from 30°C to 60°C, and (b) the Values between 70°C and 100°C were Extrapolated based on the Results from 30°C to 60°C due to the Temperature Limitations of the Tensiometer. .49
16. Fluid Level Changes due to the Evaporation Rate Difference for Graphite Nanofluid with SDS, Silver Nanofluid with SDS, and Pure Water (a) Front Sides, and (b) Back Sides (from the left: Graphite Nanofluid, Silver Nanfluid, and Water).....55
17. Size-Dependent Melting Temperature (°C) Change based on the Gibbs-Thomson Equation [30] [31], where T is the Temperature of the Nanoparticle, Tbulk the Melting Temperature of Bulk Ag, θ Surface Energy, M Atomic Mass, ΔHmMelting Enthalpy, ρ Density, and R the Diameter of the Nanoparticles [31].....57
18. Three Hypotheses for the Melting of Nanoparticles Suspended in a Solution: (a) Homogeneous Melting (HM) (b) Liquid Nucleation and Growth (LNG) (c) Liquid Skin Melting (LSM).....58
19. Modeled Geometry of Surface Melting of Silver Nanoparticles in Water [39].....61
20. (a) Schematic Diagram of the Set-Up for Boiling Experiment of Silver Nanofluid with Laser (b) Schematic Representation of Test Cell with Thermal and Optical processes.....68

Figure Page

21. TEM Images of 0.1% by Volume, 20-nm Ag Particles (a) before Heating (b) after Laser Heating in Subcooled Fluid, and (c) after Laser Heating in Saturated Fluid 71
22. Histograms of Particle Size Distributions Measured from the TEM Images in Figure 5 of (a) Particle Size Distribution before Heating (Mean = 42.9nm) (b) Particle Size Distribution after Laser Heating in Subcooled Fluid (Mean = 41.4nm), and (c) Particle Size Distribution after Laser Heating in Saturated Fluid (Mean =32.5nm) 73
23. Volume-Weighted Ag Nanoparticles (Initially 20 nm) Size Distribution Measured with Dynamic Light Scattering (DLS, Nicomp 380/ZLS) of 0.1% by Volume Nanofluid (a) before Heating (b) after Laser Heating in Subcooled Fluid, and (c) after Laser Heating in Saturated Fluid 75
24. Clathrate Structure by Presence of the Graphite Nanoparticles in Pure Water.....79
25. Typical Rankine Cycle.....82
26. Components of a Nanofluid-Based Solar Thermal System 83
27. Preparation of Silver Nanofluids in a Cycle 84
28. Schematic of Solar Thermal Storage in a House (http://solar.colorado.edu/design/hvac.html) 87

NOMENCLATURE

Q	Heat input [kW]
T	Temperature [K]
t	Time [s]
m	Mass [kg]
M	Molecular mass [mol]
[P]	Parachor
h_{fg}	Latent heat of vaporization [kJ kg^{-1}]
c	Specific heat [kJ $kg^{-1}K^{-1}$]
e	Electron constant [1.602 x 10^{-19} C]
H	Latent heat of fusion [kJ kg^{-1}]
J	Joule
N	Number of electrons in the band
u	Molecular weight of the metal [mol]
w	Lifshitz constant [eV]
R	Reflectance

Greek symbols

ρ	Density [kg m^{-3}]
φ	Volume fraction [%]
σ	Surface tension [N/m]
σ	Electrical conductivity [S m^{-1}]
Ɛ	Dielectric constant [F m^{-1}]
iω	Imaginary frequency [s^{-1}]
ω	Frequency [s^{-1}]
τ	Collision time for electrons [s]
T	Transmittance
η	Electron density (the probability of an electron being present at a specific location)
v	Specific volume [m^3 kg^{-1}]
η	Efficiency of cycle
θ	Surface energy [N/m]

Subscripts

in	Input
out	Output

sat	Saturation
nf	Nanofluid
p	Pressure
P	Particle
w	Water
f	Fluid
g	Gas
F	Fermi
e	Effective
fg	Fluid Gas
loss	Losses
vapor	Vapor generation
val	Valence band

CHAPTER 1. INTRODUCTION

Nanofluids are suspensions of nanoparticles (1-100 nm in size) in common fluids such as water, thermal oils, and other fluids. In the last few decades, adding nanoparticles to fluids has often been attempted to enhance thermal properties, especially thermal conductivity, specific heat, and convection heat transfer [1] [2] [3] [4] [5] [6] [7] [8] [9]. Motivated by these results, a number of researchers have focused on employing nanoparticles to improve the working fluid's performance in various applications [8] [9]. On the other hand, relatively few studies have been reported about changes in h_{fg} caused by the addition of nanoparticles, although h_{fg} (e.g. the energy needed to create vapor) is an important property for thermal applications [7].

Recently, h_{fg} in nanofluids has been investigated to enhance the efficiency of many applications [7] [10] [11] [12] [13] [14]. These results show that the h_{fg} of water is possibly manipulated by adding nanoparticles, as suggested by some experiments in which vapor is generated around nanoparticles by volumetric heat sources, i.e., sunlight and laser irradiation [15] [16] [17]. Although the reported 'anomalous enhancements of thermophysical properties' have largely gone unrealized, nanofluids have shown some promise for solar thermal applications [8] [9], which would be enhanced with a 'tunable' h_{fg}.

1.1 Nanofluids

Nanofluids are nanoscale colloidal suspensions containing relatively low nanomaterial concentrations [1] [2] [3] [4] [5] [6] [7] [8] [9]. Nanofluids have been considered as advanced heat transfer fluids for two decades since the suspension stability of nanoparticles is much better than micron-sized particles. Due to this advantage, it is hypothesized that clogging and settling of nanoparticles in the base fluid could be reduced, resulting in enhanced thermal and physical properties [2] [8] [9] [18]. Nanofluids' properties could be further enhanced by controlling the nanomaterial, size, shape, surfactants, and base fluid [2] [8]. Among thermophysical properties, the enhanced thermal conductivity of nanofluids is widely recognized as an important thermal property, which can significantly affect system efficiency [2] [4] [5]. The low thermal conductivity (i.e. 0.1-0.6 W $m^{-1}K^{-1}$) of conventional fluids is improved by the high thermal conductivity (10-430 W $m^{-1}K^{-1}$) of solid particles. Therefore, the addition of a small volume fraction of nanoparticles in a base fluid has been the subject of considerable research [8]. In addition, other thermophysical properties, i.e., density, specific heat, thermal expansion coefficient, viscosity, and thermal conductivity have also been studied to increase the system efficiency [2] [4] [12]. However, there are still several issues (i.e. long-term stability and reproduction of experimental results) to be solved.

1.2 Latent Heat of Vaporization in Pure Water

The random movements of liquid molecules packed closely together cause molecules to collide with each other [19]. These movements become very intense as

temperature increases. Therefore, the bonds between liquid molecules are broken and the liquids become gases. This is called the boiling point of fluids. The boiling point is highly related to the strength of the bonds [19]. The boiling point of pure water is relatively high due to the strong attractions afforded by the hydrogen bonds compared with the other types of bonds. Also, the latent heat of vaporization in water is high due to the strong hydrogen bonds. Usually, a large quantity of thermal energy is needed for vaporization. This amount of thermal energy is called h_{fg}, which is used in breaking the hydrogen bonds to leave from the water surface to the air. Thus, h_{fg} is highly related to the strength and number of bonds [19].

1.3 Historical Attempts to Manipulate the Latent Heat

As shown in Table 1, Ameen et al. [7] presented an h_{fg} increase for Pt nanofluids compared to that of pure water as a function of the volume fraction (%) and the nanoparticle size. Their research was based on a molecular dynamics (MD) simulation supplemented with limited experimental data for alumina nanofluids. An increase in h_{fg} was noted in aqueous nanofluids with an increase in the volume fraction and with a decrease in the nanoparticle size as shown in Fig. 1. From these results, Ameen et al. [7] concluded that the influence of the nanoparticle volume fraction was the dominant influential parameter as compared to nanoparticle material and size. In addition, they discussed that the increase in h_{fg} in nanofluids could possibly be caused by extra bonds between water molecules and nanoparticles. That is, in order to break the extra bonds, extra energy is required during phase change, which leads to the h_{fg} increase.

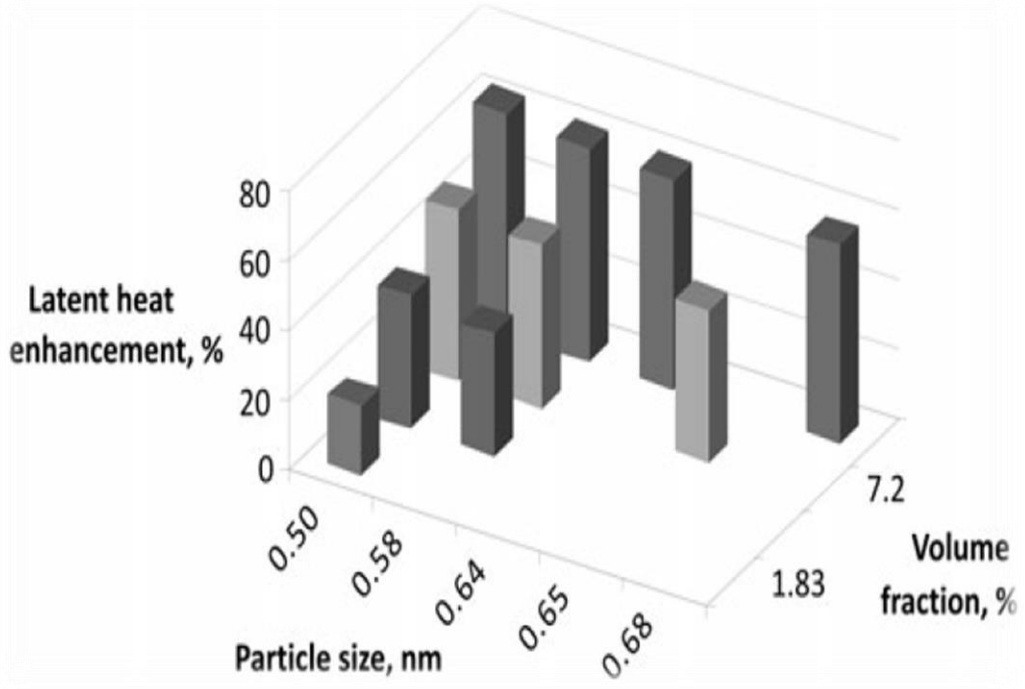

Figure 1. The Enhancement of h_{fg} of Water as a Function of the Volume Fraction and the Platinum Nanoparticle Size based on Molecular Dynamics (MD) Simulations **[7]**

In addition, Chen et al. [11] indicated that the surfactant Polyvinylpyrrolidone (PVP) could enhance the evaporation rate of deionized water droplets due to the reduction of the surface tension of water. Since much of the nanofluids literature employs surfactants, a reduction in h_{fg} of up to 10% can be attributed to the presence of surfactants [10] [11].

Table 1 Review of Latent Heat of Nanofluids **[20]**

Year	Authors	Nano fluid	Volume fraction (%)	Description	Surfactant (%)	Latent heat (kJ kg^{-1})
2010	Ameen et al. [7]	Pt	1.83	An increase in h_{fg} is noted with an increase in the volume fraction and with a decrease in the size of the nanoparticles.	Not stated	+20%
			4			+35%
			7.2			+45%
		Al_2O_3	0.5		Not stated	+7%
			1			+15%
			2			+22%
2010	Chen et al. [11]	Laponite	0.5	The results show that adding nanoparticles and PVP in deionized water can change evaporation rates and $h_{fg.}$	0	+10%
		Ag	0.04		0	Increase
			0.05		1	Increase
		Fe_2O_3	0.05		1	Increase
2011	Zhu et al. [12]	Al_2O_3	0.1	Explored aqueous Al_2O_3 nanofluids with different sizes at various concentrations to investigate thermophysical properties. h_{fg} is proportional to increasing volume fraction, but h_{fg} is also inversely proportional to increasing particle size	Not stated	Increase
			0.5			Increase

2013	Harikrishnan et al., [13]	TiO_2	0.1 0.2 0.3	Dispersed nanoparticles in palmitic acid enhanced the heat transfer characteristics of palmitic acid including the latent heat.	Not stated	+6.18% +12.37% +20.11%
2014	Mehregan et al. [14]	-	-	Presented a new theoretical equation for h_{fg} in nanofluids	-	-
2014	Lee et al. [10]	Ag Graphite	0.1 0.1 0.1 0.1	h_{fg} of water* can be increased or decreased by aqueous graphite and silver nanofluids with volumetric heat source (i.e. laser or sunlight)	0 1 0 1	-23% -34% +36% +32%

* Latent heat of vaporization in water: 2257 kJ/kg

This is similar to other studies that have examined the effect of surfactants on surface tension and corresponding impacts on boiling heat transfer [21]. In addition, Chen et al. reported there was only a slight change in h_{fg} for a silver (Ag) nanofluid without PVP, however, h_{fg} increased as the particle concentration increased and the evaporation rate decreased. On the other hand, h_{fg} for a Ag nanofluid with PVP increased with increasing particle concentration due to additional interactions between nanoparticles and water molecules, i.e., the evaporation rate decreased with increasing particle concentration. In general, Chen et al. [11] found that adding nanoparticles such as Laponite, Ag, and Fe_2O_3 in deionized water could change the evaporation rates and h_{fg} as shown in Table 1. Also,

Zhu et al. [12] presented measured thermophysical properties, such as the viscosity, surface tension, thermal conductivity, saturation vapor pressure, and h_{fg} of aqueous alumina nanofluids with different size nanoparticles at volumetric concentrations of 0.1% to 0.5%. In their paper, the influences of the particle size, particle volume concentration and temperature on the thermophysical properties were investigated. For example, h_{fg} was proportional to increasing volume fraction, but h_{fg} was also inversely proportional to increasing particle size. Harikrishnan et al. [13] reported that dispersed TiO_2 nanoparticles in palmitic acid could be employed for enhanced heat transfer characteristics of palmitic acid, including the latent heat. Therefore, based on their good thermal stability and thermal reliability, newly prepared TiO_2 nanofluids could be considered as additives to make efficient phase-change materials (PCMs) for solar water heating systems. Recently, Mehregan et al. [14] proposed a new theoretical equation, an expression for h_{fg} for nanofluids:

$$(\rho h_{fg})_{nf} = (1-\varphi)\rho h_{fg} + \left(T_{bf}/T_{b,s} * \varphi\, \rho_s h_{fg,s}\right) \quad (1)$$

where T_{bf} is the boiling point of the base fluid, the subscripts nf represents nanofluid and s nanoparticles, and no subscript designates the base fluid. Mehregan et al. proposed that h_{fg} is a function of both the base fluid and the nanoparticles. That is, h_{fg} of nanofluid is treated as a solid-fluid mixture rather than as a homogeneous fluid. Thus, h_{fg} can be derived by considering the density, the boiling temperatures of the base fluid and nanoparticles, and h_{fg} of both the base fluid and of the nanoparticles. Mehregan et al. [14] numerically

investigated the evaporation behavior of nanofuel droplets using a general transport equation, and compared the numerical results with available experimental data of nanofluid evaporation characteristics to propose the above correlation to approximate h_{fg} in nanofluid. It indicated that h_{fg} is highly dependent on the type of the nanoparticles. This was the first work to propose a formula for h_{fg} in nanofluids as a function of density, volume fraction, and boiling temperatures of the nanoparticles and of the base fluid. Mehregan et al., however, mentioned that further investigation is still required to improve this relation because it is the first attempt to propose a formula to approximate a nanofluids' h_{fg}. Finally, Lee et al. [10] recently presented experimental data for h_{fg} for 0.1% by volume, 30-nm graphite and 20-nm silver nanofluids with and without 1% surfactant. The h_{fg} results were inspired by other studies [15] [16] [17], which showed that vapor generation around nanoparticles in water by volumetric heat sources i.e., concentrated sunlight or a focused laser beam, could be realized in subcooled and saturated water. Based on those results, Lee et al. conducted experiments with a laser heat source to investigate h_{fg} in aqueous graphite and silver nanofluids. The results indicated that h_{fg} for graphite nanofluids can be increased, and h_{fg} for silver nanofluids can be decreased by ±30%-36%, relative to h_{fg} for pure water. According to Table 2, all previous h_{fg} studies in aqueous nanofluids always showed an increase in $h_{fg,}$ compared to that for pure water (2257 kJ kg^{-1}) due to the addition of nanoparticles. Lee et al., however, reported a decrease in h_{fg} for silver nanofluids. This indicates that the materials involved are critical in controlling h_{fg}. If these materials and results can be scaled up, such nanofluids can potentially be employed for solar steam generators or directly irradiated latent heat storage systems with tunable h_{fg} as a function of nanoparticle material.

Table 2 Values of Latent Heat of Vaporization in Aqueous Nanofluids

Year	Authors	Nanofluid	Volume fraction (%)	Latent heat of Vaporization (kJ kg^{-1})
2010	Ameen et al. [7]	Pt	1.83	2708
			4	3046
			7.2	3272
		Al_2O_3	0.5	2414
			1	2595
			2	2753
2010	Chen et al. [11]	Laponite	0.5	2482
2014	Lee et al. [10]	Ag	0.1	1633
		Graphite	0.1	3529

* Latent heat of vaporization in water: 2257 kJ/kg

1.4 Volumetric Solar Thermal Collector

A conventional solar thermal collector, a device for capturing solar radiation with a flat plate or evacuated tube, harvests heat energy by absorbing sunlight on the collector surface.

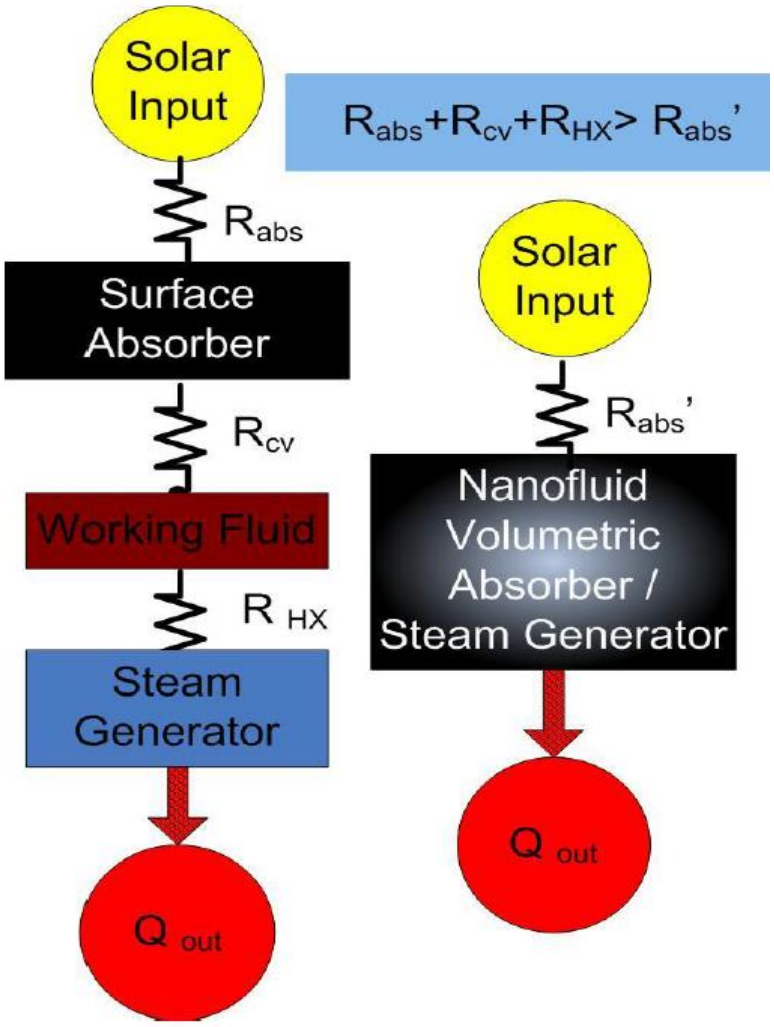

Figure 2. Thermal Resistance Network of a Conventional Solar Thermal Plant and a Nanofluid-Based Volumetric Solar Thermal Plant **[15]**.

However, nanofluid-based volumetric solar thermal collectors, which contain very small amounts of nanoparticles (<1% by volume) in pure water, have received interest because they harness solar radiant energy more efficiently by capturing the sun's energy with improved optical and thermal properties as compared to conventional solar thermal collectors [3] [9] [15] [16] [22]. The efficiency of a solar thermal system is related to the

number of energy conversion steps. Compared to a conventional solar thermal collector, a nanofluid-based volumetric solar collector can increase the efficiency by reducing the energy conversion steps as shown in Fig. 2. As will be shown later in this chapter, the ability to increase or descrease h_{fg} could enable more useful application of volumetric solar collectors.

1.5 Motivation

Recent work on light-induced vapor generation of aqueous nanofluids reveals that a large portion of the input light is not transferred to the surrounding water, due to the low thermal conductivity of water vapor surrounding the nanoparticles as shown in Fig. 3. This is believed to act as a thermal barrier between the nanoparticles and the nearby liquid water. This indicates that under light-induced heating, nanoparticles act as heat sources which are not in equilibrium with their surroundings [17].

Therefore, if thermal losses are insignificant from the test samples, the total energy from the light would be absorbed into the nanoparticles and vapor is generated around nanoparticles as shown in Fig. 4 instead of transferring to the liquid water [16] [17].

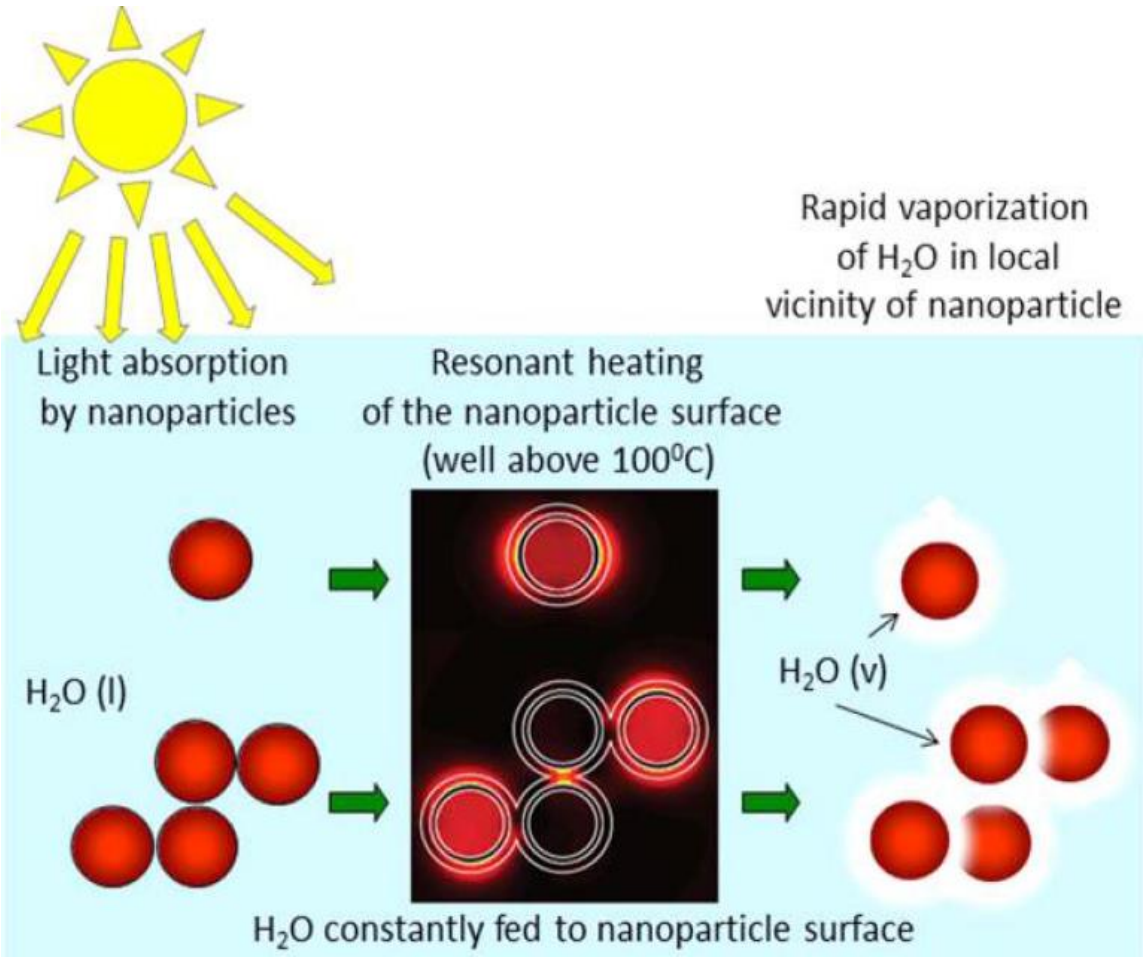

Figure 3. Schematic of Solar Steam Generation based on Nanoparticles **[17]**

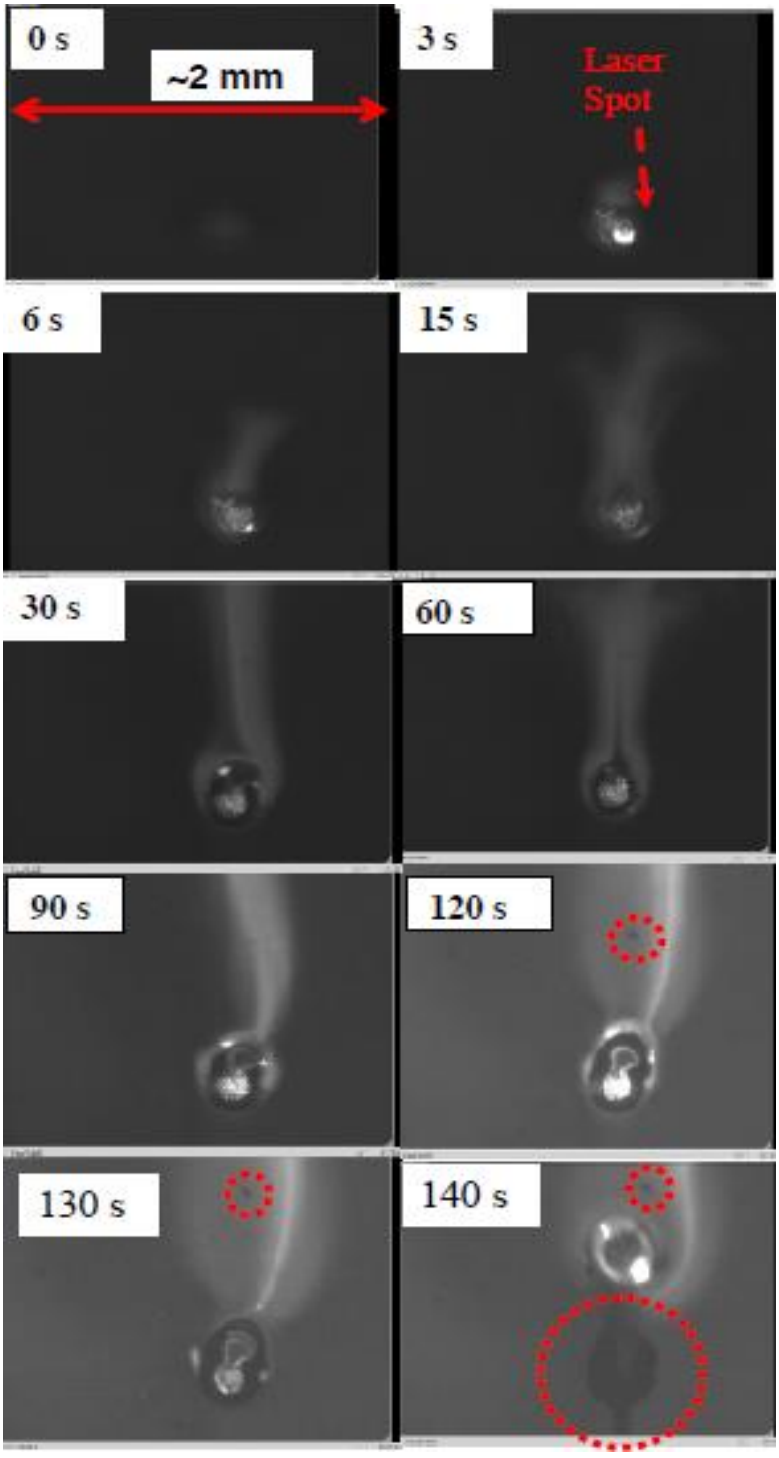

Figure 4. Vapor Generation around Graphite Nanoparticles in Water with a Laser Irradiance of 770 W/cm^2. Dashed Circles Indicate Separated High Concentrations of Graphite Nanoparticles **[16]**.

From this, the local temperature of nanoparticles could increase much higher than the temperature of the nearby liquid water. It may therefore be possible to affect the thermal properties of nanofluids or the melting behavior of nanoparticles in water, including. the latent heat of vaporization (h_{fg}). Among other applications such as steam generation, h_{fg} is an important property in determining how effectively a liquid can regulate the internal temperature of a living organism.

Also, a stable system can be achieved since the system operates with both constant temperature and constant pressure. Therefore, if h_{fg} in water is increased by adding a small amount of nanoparticles, a large amount of energy could be stored via latent heat storage because water has both a high h_{fg} and a high heat capacity.

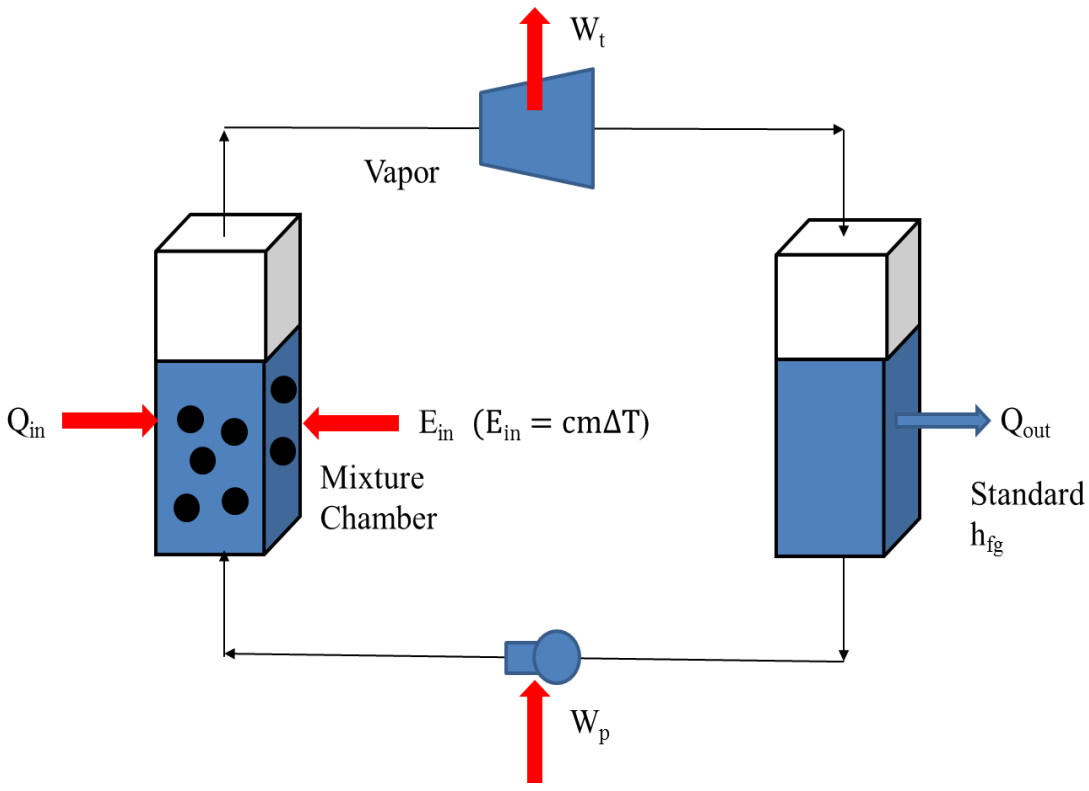

Figure 5. Suggested Volumetric Solar Thermal System Using Nanofluids

In addition, if h_{fg} in water is decreased, more steam could be generated from the same heat input to a volumetric solar thermal collector as shown in Fig. 5. If h_{fg} is increasd by adding nanoparticles, some energy is used for the interactions between nanoparticles and water molecules and these interactions could be higher than the broken hydrogen bonds due to placing nanoparticles inside pure water. That is, less heat output could be achieved than the value of pure water. Also, if h_{fg} decreased by adding nanoparticles, the interactions between nanoparticles and water molecules could be prevented by van der Walls interaction change due to melting, thus the broken hydrogen bonds could not be compensated. Therefore, more heat output (vapor) could be possible. The details will be discussed in Chapter 5.

1.6 Research Goals

The goals of the research are to investigate the variation of h_{fg} in silver and graphite aqueous nanofluids, with both volumetric and surface heat sources. The main purpose of this research is to determine if h_{fg} in aqueous nanofluids can be increased or decreased, compared to the h_{fg} of pure water. A secondary goal is to show how manipulating h_{fg} in this way can be applicable to solar thermal energy harvesting or energy storage. To make it clear, the challenges of this research are the following:

- Is there any difference when surface heating and volumetric heating is used for h_{fg} in nanofluids?
- Is there sufficient confidence in the accuracy of the experimental h_{fg} measurements?

- Does the type of nanofluid affect the variation of h_{fg}?
- Is the variation of h_{fg} in nanofluids possible to be employed for real-world applications such as latent heat storage systems and solar thermal collectors?

The above questions are addressed in the following chapters in this dissertation. The next chapter will present the experimental results of h_{fg} in aqueous nanofluids. This will include the experimental methods, procedure, and results. Chapter 3 presents theoretical approaches to support the experimental results. Chapter 4 suggests possible nanoscale mechanisms to predict how h_{fg} can be altered. Finally, Chapters 5, 6, and 7 discuss applications in solar thermal energy, the conclusions and suggestions for future work.

CHAPTER 2. EXPERIMENTAL INVESTIGATION OF THE LATENT HEAT OF VAPORIZATION IN AQUEOUS NANOFLUIDS

Recently, Ameen et al. [7] proposed the enhancement of h_{fg} in platinum and aluminum oxide nanofluids by MD simulations and limited experiments where the nanofluids were heated through conventional surface heaters. However, there are limits to investigating h_{fg} with surface heating since it is evident that volumetric vapor generation occurs around nanoparticles in aqueous nanofluids [16] [17]. Volumetric heating sources, such as a laser, sunlight, or an electrically heated hot wire which delivers the thermal energy by directly contacting nanoparticles, appears to more fully utilize the dispersed nature of nanoparticles inside a test cell compared to surface heat sources. In particular, it has been shown that the vapor can be locally created around nanoparticles, without heating the entire bulk of the fluid [16] [17]. To obtain a better fundamental understanding of this phenomenon, an experimental quantification of h_{fg} is required for the volumetric vapor generation in aqueous silver and graphite nanofluids because these nanoparticles showed better results than other nanoparticles in previous work [16].

2.1 Experimental Setup and Procedure

The h_{fg} of fluids is determined by measuring vapor generation and the heat input supplied during the time of observation. Figures 6(a) and (b) describe the experimental set-up used in this study for measuring vapor generation with a laser and an electrically heated Ni-Cr resistance wire.

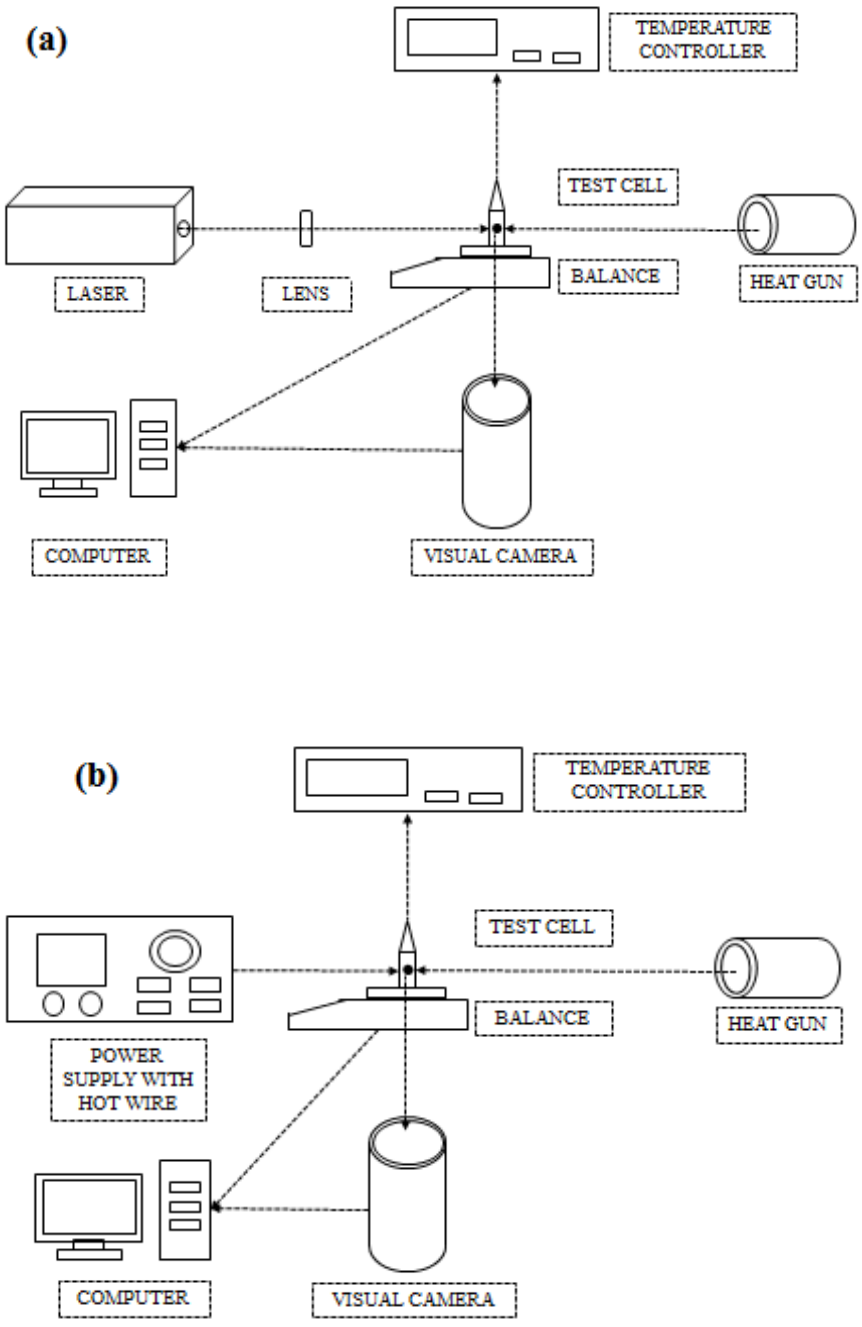

Figure 6. Experimental Setup for Measuring the Latent Heat of Vaporization in Nanofluids with (a) Laser-Based Heating, (b) Hot Wire-Based Heating

This experimental set-up represents a refined, transient version of a previous experimental study [15]; photographs of the system are shown in Fig. 7.

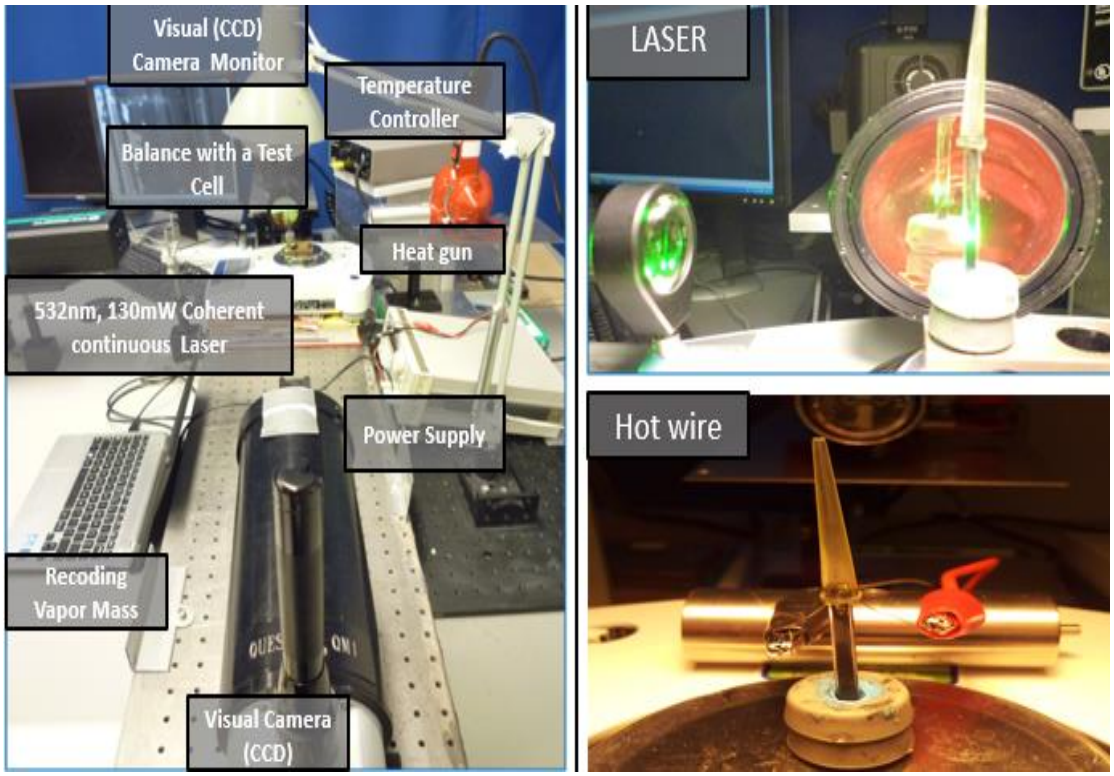

Figure 7. Experimental Setup – Taken Using a Digital Camera

In this set-up, a thin-walled 2mm x 2mm square, quartz cuvette is filled with one of the following samples: graphite nanofluid (0.1% by volume, 30nm in size), silver nanofluid (0.1% by volume, 20nm in size), and pure water with surfactants, which are necessary to stabilize the nanoparticles in water. Nanofluids could be prepared by the "one-step" method or the "two-step" method. The one-step method consists of synthesizing nanoparticles in the base fluid by means of a chemical method. The two-step method is that nanoparticles

are prepared in the form of powders first, then suspended in the base fluid [10] [15]. In this dissertation, the two-step method was employed to prepare aqueous silver and graphite nanofluids. The cuvette containing the nanofluid sample was mounted on a sensitive mass balance (Mettler Toledo, AB265S, 0.01mg accuracy) to measure the mass of the remaining liquid of the test samples with a continuous laser (532nm in wavelength, 130mW in power output) which is focused through a 40-mm focal length positive lens as shown in Fig. 7, and a K-type thermocouple (Omega, 1.574 mm in diameter) was immersed in the nanofluid to record the temperature of the test samples. In addition, bubble formation was observed visually with a Retiga (EXi Fast) 1.4 megapixel charge-coupled device (CCD) camera to determine the boiling in the test samples. Figure 8 illustrates three different experimental setups to determine h_{fg} in our samples and the experimental procedure. The boundaries of the cuvette are either kept at a constant temperature (of just below 100°C) using a heat gun, or are insulated with rubber pipe type insulation (Industrial Thermo Polymers Lim, 38mm thickness). This variety of conditions (volumetric laser heating, and hot-wire heating with and without external heating) was employed in order to confirm the experimental results were not artifacts of the method used. That is, these tests seek to determine if the presence and type of nanoparticles lead to the same changes in the observed h_{fg} for all cases. Optical losses during the laser-heated experiments were estimated to be 3%, while thermal losses from the well-insulated sample were estimated to be 1%. The detailed uncertainty estimates are provided in Appendix A.

(a) **(b)** **(c)**

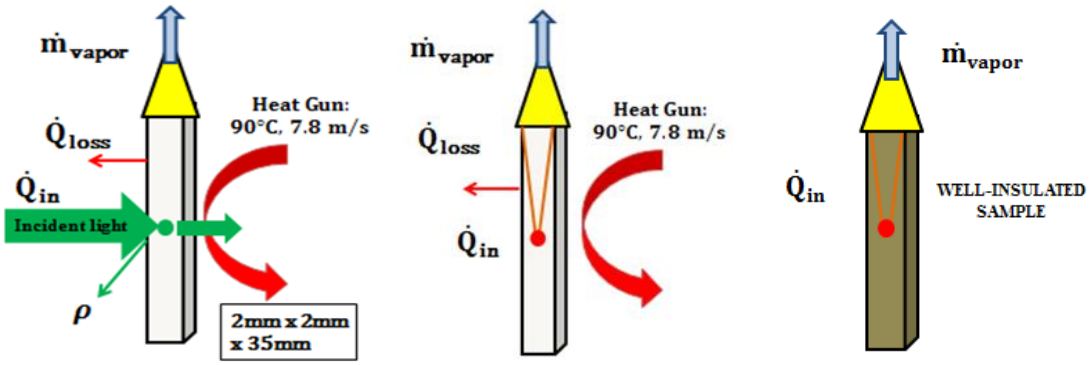

(d)

Time	Action
0 s	Turn on heat gun
60 s	Turn on primary heat source
1200 s	Turn off primary heat source and heat gun

Figure 8. Schematic Diagram for (a) Laser and a Heat Gun, (b) A Hot Wire and a Heat Gun, (c) a Hot Wire and Well-Insulated Sample, (D) Boiling Experiments Procedure

(a)

(b)

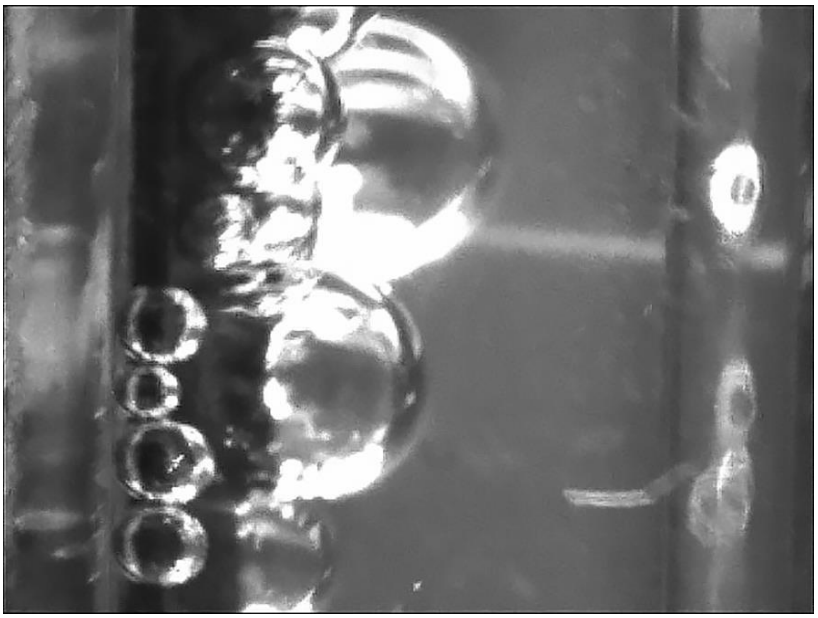

Figure 9. Visual Images Exposed to Laser Beam (a) Prepared Nanofluids with Pure Water (b) Bubbles in Test Cells during the Experiments

For the laser-based experiments, all the test cells were black-backed to ensure all light was absorbed. Therefore, the scattering of light in the test sample was ignored as it was absorbed either in the fluid or on the backing regardless of the fluid. Note: the assumption that no light leaves the cuvette was confirmed with measurements using a laser power thermopile sensor (Coherent, PM30V1Q). A cap with a small opening was utilized which allows for the insertion of thermocouples to measure the temperature of the nanofluids and sustains a test fluid at saturation pressure while conducting the experiment. During the tests, all samples (shown in Fig. 9(a)) were sufficiently heated to create vapor as is demonstrated in the characteristic visual image of Fig. 9(b). The entire setup was then recorded throughout the experiments with a visual camera to observe vapor bubbles in fluids to check volumetric boiling, while conducting the experiments and based on The bubble formation details as described in previous work [15].

2.2 Experimental Method

To measure the vapor mass, the fluid mass was measured before and after the experiments. A total observation time of 20 minutes was used, which ensured a measurable mass change without lowering the liquid column below the heated region. In order to consider the boiling effect, input from the heat gun only was also run to investigate the evaporation effect of our setup to determine repeatability and estimate the test uncertainty (~15%) [10] [15]. The uncertainty of the experimental data was calculated based on a level of confidence of 95%. The detailed uncertainty estimates are provided in Appendix B. The h_{fg} results indicated that the changes in h_{fg} were a profound function of the type of

nanoparticle, regardless of whether a surfactant was present or not. The values for h_{fg} were determined from the experimental measurements by [10]:

$$h_{fg} = \frac{\int_0^{t_F} \dot{Q}_{in}\, dt - \int_0^{t_F} \dot{Q}_{loss}\, dt}{\int_0^{t_F} \dot{m}_{vapor}\, dt} \tag{2}$$

where $\dot{m}_{vapor}$ is the mass flow rate of vapor generation (kg/s), t the time (sec), $\dot{Q}_{in}$ the rate of heat input (kW), which was measured by the power thermopile sensor (Coherent, PM30V1Q), and $\dot{Q}_{loss}$ the thermal losses (kW), which were calculated based on the temperature of the nanofluid and the cuvette boundary:

$$\int_0^{t_F} \dot{Q}_{loss}\, dt = hA(T_{nf} - T_{air}) \tag{3}$$

where h is the convective heat transfer coefficient, A the surface area of the cuvette, T_{nf} the temperature of the nanofluid, and T_{air} the temperature of the air. The convective heat transfer coefficient was obtained after calculation of the Reynolds (1184) and Nusselt (20.32) numbers [23]:

$$\mathrm{Re} = \frac{v_{air} L}{\nu}$$

$$\mathrm{Nu} = \frac{hL}{k} = 0.664 \mathrm{Re}^{0.5} \mathrm{Pr}^{\frac{1}{3}} \tag{4}$$

where v_{air} is the air velocity (7.8 m/s) [15], L the characteristic linear dimension (0.0035 m), ν the kinematic viscosity (23.06 x 10^{-6} m^2 s^{-1}), k the thermal conductivity (0.0314 W m^{-1} K^{-1}), and Pr the Prandtl number (0.703) [23]. Solution of Eq. (9) led to an estimated cnvective heat transfer coefficient of h = 182 W m^{-2} K^{-1}. Therefore, the thermal losses (1.45 J) using Eq. (8) for the experiments shown in Figs. 8 (a) and 8 (b) can be calculated for the 20-minute observation time. The negligible thermal loss for the experiment shown in Fig. 8 (c) was obtained by considering only heat conduction. The details for the uncertainty calculations are provided in Appendices A and B.

Based on Eq. (2), $m_{vapor} = \int_0^{t_F} \dot{m}_{vapor}\, dt$ can be identified as an important factor in determining h_{fg} (as compared with the other controlled variables, i.e., heat input and thermal losses), particularly since the latent heat results were similar for the three experimental set ups as shown in Tables 3-5. Since the evaporation of the fluid also occurs due to the presence of the heat gun, in order to only consider the boiling effect from the laser or hot wire, the results from both the laser (hot wire) and the heat gun were normalized by the amount of evaporation resulting from the heat gun only, i.e., the background vapor mass generation. That is, the heat gun experiments with no light input were also run to find the amount of evaporation resulting from the saturation temperature boundary condition [10].

Table 3 The Values of All Three Terms on the RHS of Eq. (27), for the Laser Experiment Shown in Fig. 8 (a), Where t_F = 20 min and 0.1% Volume Fraction Nanofluid.

	Q_{in} (J)	Q_{loss} (J)	Vapor mass generation w/ 1% SDS (mg)	Background vapor mass generation w/ 1% SDS (mg)	Vapor mass generation w/o SDS (mg)	Background vapor mass generation w/o SDS (mg)
Pure water	146	1.45	68 ± 7	18 ± 1	63 ± 7	15 ± 1
Graphite nanofluid	137	1.45	41 ± 3	24 ± 2	38 ± 3	20 ± 2
Silver nanofluid	120	1.45	79 ± 10	22 ± 2	72 ± 9	19 ± 2

These background/control test results are given in Tables 3-4, and the net vapor mass generation (the difference between the total vapor mass generation and the background vapor mass generation) was used in Eq. (2). Since the heat gun was not used for the well-insulated sample in Fig. 8(c), no background vapor mass generation is given in Table 5 for that case. In addition, for the hot wire-based experiments using an insulated test cell, a different heating power (680mW) was applied to reach the boiling point in 1 min without a heat gun, and the observation time was 5 min.

Table 4 The Values of All Three Terms on the RHS of Eq. (2), for the Hot Wire Experiment with a Heat Gun Shown in Fig. 8 (b), Where t_F = 20 min and 0.1% Volume Fraction of Nanofluids.

	Q_{in} (J)	Q_{loss} (J)	Vapor mass generation w/ 1% SDS (mg)	Background vapor mass generation w/ 1% SDS (mg)	Vapor mass generation w/o SDS (mg)	Background vapor mass generation w/o SDS (mg)
Pure water	148	1.45	73 ± 7	18 ± 1	67 ± 7	15 ± 1
Graphite nanofluid	148	1.45	46 ± 3	24 ± 2	43 ± 3	20 ± 2
Silver nanofluid	148	1.45	87 ± 10	22 ± 2	81 ± 9	19 ± 2

Therefore, the vapor mass generation in Table 5 was different from the others in Tables 3 and 4, but the resulting values of h_{fg} were similar. Therefore, interactions between the nanoparticles and water molecules apparently differ, depending on the nanoparticle material. Also, as shown in Tables 3-5, the presence of a surfactant (SDS) in the fluids causes a reduction of 6-10% in h_{fg} for the nanofluids. However, the results for the net vapor mass generation (m_{vapor}) show that even though m_{vapor} for pure water with a surfactant is greater than that for pure water without a surfactant, m_{vapor} is still lower than that for silver nanofluid.

Table 5 The Values of All Three Terms on the RHS of Eq. (2), for the Hot Wire Experiment with a Well-Insulated Sample Shown in Fig. 8 (c), Where t_F = 5 min and 0.1% Volume Fraction of Nanofluids (Zero Background Vapor Mass Generation)

	Q_{in} (J)	Q_{loss} (J)	Vapor mass generation w/SDS (mg)	Vapor mass generation w/o SDS (mg)
Pure water	204	0.006	98 ± 7	89 ± 7
Graphite nanofluid	204	0.006	61 ± 3	58 ± 3
Silver nanofluid	204	0.006	130 ± 10	118 ± 9

2.3 Experimental Results and Discussion

Table 6 gives the results of the laser-based h_{fg} measurements for graphite and silver nanofluids calculated from Eq. (2). $\dot{Q}_{in}$ and $\dot{m}_{vapor}$ were measured by the power meter and the balance, respectively. Also, $\dot{Q}_{loss}$ was calculated based on the temperature of the nanofluid and the cuvette boundary, and was approximately 1% of $\dot{Q}_{in}$. In these experiments, a graphite nanofluid (0.1% particles by volume, 30nm particle diameter) showed a 36% increase in h_{fg} and a silver nanofluid (0.1% particles by volume, 20nm particle diameter) showed a 30% decrease in h_{fg} compared to the standard value for pure water.

Table 6 The Results of h_{fg} in Fluids Using a Laser

	h_{fg} with 1% surfactant (kJ/kg)	h_{fg} without 1% surfactant (kJ/kg)
Pure water	2132 ± 288	2287 ± 309
Graphite/water nanofluid	3341 ± 515	3529 ± 543
Silver/water nanofluid	1492 ± 233	1633 ± 255

. Standard value of Latent Heat of Vaporization: 2257 kJ/kg

The uncertainty in these measurements was calculated following standard texts with 95% confidence level [24], resulting in an estimated uncertainty in h_{fg} of ± 15% for the laser-based experiments. To ensure these results are not an artifact of the laser heating method or of the boundary condition imposed by the heat gun, the same samples were also tested with the more widely used hot wire heating method [10], as shown in Fig. 10 for a well-insulated sample. To begin with, hot wire-based (130mW) experiments with a heat gun were conducted. The results as shown in Table 7 indicated only slight differences from the values measured during the laser experiments in Table 6. The difference is partly due to the reflection in the cuvette filled with fluids for the laser experiments since the reflectance was approximately 3.6 %, which is given by Fresnel equation in Eqs. (5) and (6) with the reflective index of fused quartz glass (1.46) and air (1.0) at 532nm wavelength for all fluids [10] [15]:

$$R_{glass} = \frac{(n_{glass} - n_{air})^2}{(n_{glass} + n_{air})^2} \quad (5)$$

where R is the reflectance, and n the refractive index. The subscripts glass and air represent the test cell material and air, respectively.

Table 7 The Results of h_{fg} in Fluids Using a Hot Wire

	h_{fg} with 1% surfactant (kJ/kg)	h_{fg} without 1% surfactant (kJ/kg)
Pure water	2022 ± 243	2177 ± 226
Graphite/water nanofluid	3204 ± 368	3392 ± 390
Silver/water nanofluid	1679 ± 201	1820 ± 218

Note that no heat gun is used in the arrangement of Fig. 10. Table 9 shows that the hot wire-based experiments using an insulated test cell confirmed the results from both laser heating (Table 7) and hot-wire heating (Table 8). In these experiments, in order to reach the boiling point in 1 minute without a heat gun, a different heating power (680mW) based on the energy balance in Eq. (2) was applied, but the time to reach boiling conditions was different from the previous experiments. Therefore, the vapor mass generated from the

nanofluid only after reaching the boiling point was recorded. As a result, additional vapor generation from evaporation was not included in the results, but the h_{fg} values obtained without the use of a heat gun are within ± 6 % of the other results.

$$R_{total} = R_{glass} + \frac{T_{glass}^2 R_{nf}}{1 - R_{nf} R_{glass}} \tag{6}$$

where T (1.0) is the transmittance, and R_{nf} (0.0005) the nanofluid reflectance. The subscripts glass and nf represent the test cell material and nanofluid, respectively.

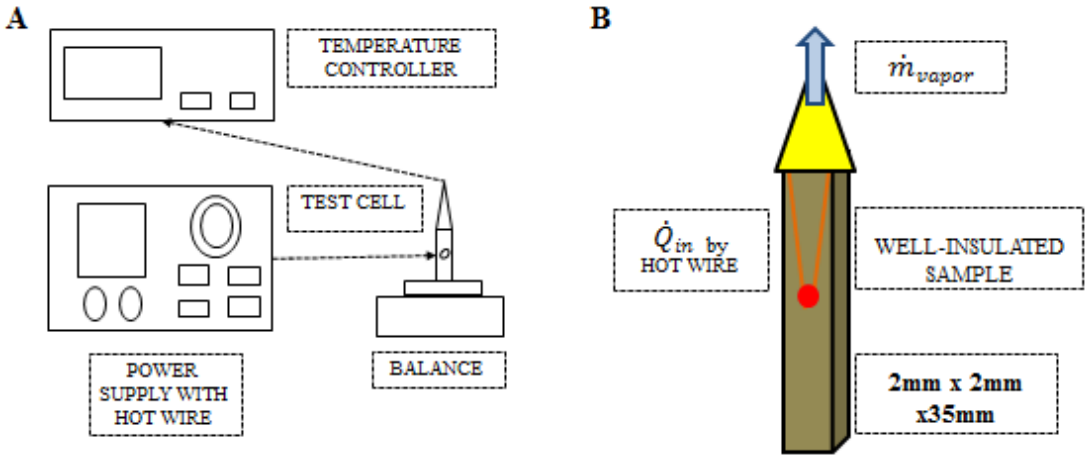

Figure 10. (A) Schematic Diagram of the Experimental Set-up for Measuring the Latent Heat of Vaporization in Nanofluids using a Hot Wire with Electrical Source. (B) Schematic Representation of Well-Insulated Boiling Test Cell to Reduce Heat Loss by Convection and Radiation.

Hence, hot wire-based experiments using an insulated test cell confirmed the original results from laser heating.

Table 8 The Results of h_{fg} in Fluids without a Heat Gun

	h_{fg} with 1% surfactant (kJ/kg)	h_{fg} without 1% surfactant (kJ/kg)
Pure water	2090 ± 190	2299 ± 209
Graphite/water nanofluid	3358 ± 316	3498 ± 329
Silver/water nanofluid	1568 ± 149	1728 ± 164

Moreover, h_{fg} of nanofluids with and without 1% surfactant (commonly used for stabilizing nanoparticles) was obtained to investigate the effect of the surfactant [10]. As shown in Fig. 11, vapor mass generation of aqueous nanofluids and pure water with and without SDS were different while conducting the experiments. These experiments were repeated five times to reduce the error of the tests, and averaged to determine the repeatability [24].

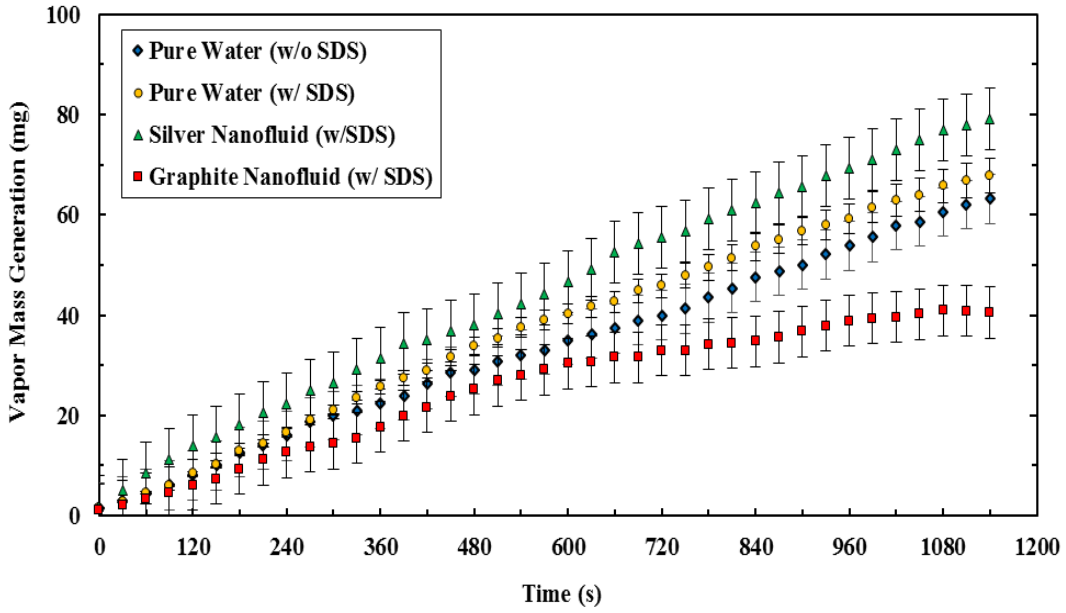

Figure 11. Vapor Mass Generation based on Laser and a Heat Gun Experiment as a Function of Time for Pure Water with and without Surfactant (SDS), 0.1% by Volume, 20-nm Silver Nanofluid with 1% Surfactant, and 0.1% by Volume, 30-nm Graphite Nanofluid with 1% Surfactant

Based on the results in Fig. 11, the variations in h_{fg} for graphite and silver nanofluids are largely caused by the presence and type of nanoparticles rather than the surfactant. The h_{fg} in fluids with 1% surfactant shows marginally lower values than the samples without 1% surfactant. This is a well-described phenomenon, and is due to the fact that a surfactant in fluid alters the surface tension [25]. In general, bubbles generated during boiling find it difficult to escape the interface between the fluid/air boundary due to surface tension in fluid. However, the surfactant reduces the surface tension by disturbing the interaction energy at the interface, thus allowing bubbles to leave [26]. Based on the results in Table

6-8, it is hypothesized that the type of nanoparticle has a crucial impact on vapor generation during boiling. Analogous to surfactant, when nanoparticles are placed in water, hydrogen bonds are broken to make room for the nanoparticles [19].

Subsequently, new hydrogen bonds around nanoparticles are formed due to the layering of water molecules [10] [19]. Therefore, the new hydrogen bonds and the additional interactions between nanoparticles and water molecules could be replaced for those broken hydrogen bonds. That is, those interactions could cause an increase in h_{fg}. Recently, M. Mehregan et al. proposed a formula for nanofluids' h_{fg}, given earlier as Eq. (1). [27] Also, C. Gerardi et al. [27] presented the *effective volume fraction* φ',

$$\varphi' = \varphi[1 + hS_A\rho_P] \tag{7}$$

where φ is the volume fraction, h the thickness of the ordered layer, S_A the Brunauer-Emmett-Teller (BET) surface area, and ρ_P the density of the nanoparticles [14]. Based on Eq. (6) with the effective volume fraction change based on existing parameters [10] [27], h_{fg} of 0.1% by volume aqueous graphite (hydrophobic) nanofluid could be increased up to ~2%. However, this ignores various mechanisms, including the density change of water and nanoparticles, the localized (volumetric) high fluid temperatures surrounding the nanoparticles caused by laser absorption (the hydrophobic interaction highly depends on temperature), and size-dependent boiling point changes. Therefore, a considerable increase of h_{fg} could be realized if such additional mechanisms are included. Furthermore, again based on Eq. (6), the h_{fg} of 0.1% by volume aqueous silver nanofluid could be decreased

up to ~1%. In addition, based on a Hamaker constant calculation, the surface melting of silver nanoparticles in water prevents interactions between water molecules and silver nanoparticles [10]. Therefore, the broken hydrogen bonds could not be replaced by those interactions when surface melting of silver nanoparticles occurs. Therefore, a decrease in h_{fg} in silver nanofluid could also be realized.

The results in Tables 6-8 motivated an extension of the original experiments [10]: investigate the effects of nanoparticle volume fraction and size on h_{fg}. To obtain a better fundamental understanding of this phenomenon, this section reports an experimental quantification of h_{fg} for volumetric vapor generation in aqueous nanofluids in order to investigate the mechanism of the decreased and increased h_{fg} in the nanofluids using laser-based experiments. As shown in Figs. 12(a) and 12(b), volume fractions ranging from 0.005% to 2% of aqueous nanofluids were prepared with 30-nm±2nm and 100-nm±2nm graphite nanoparticles, and 20-nm±2nm, 50-nm±2nm, and 100-nm±2nm silver nanoparticles.

These nominal diameters were measured by Dynamic Light Scattering (DLS, Nicomp 380ZLS). For the graphite nanofluids shown in Fig. 12 (a), h_{fg} gradually increases with increasing concentration, up to 1% volume fraction, and then decreases thereafter due to highly unstable and agglomerated nanoparticles.

(a)

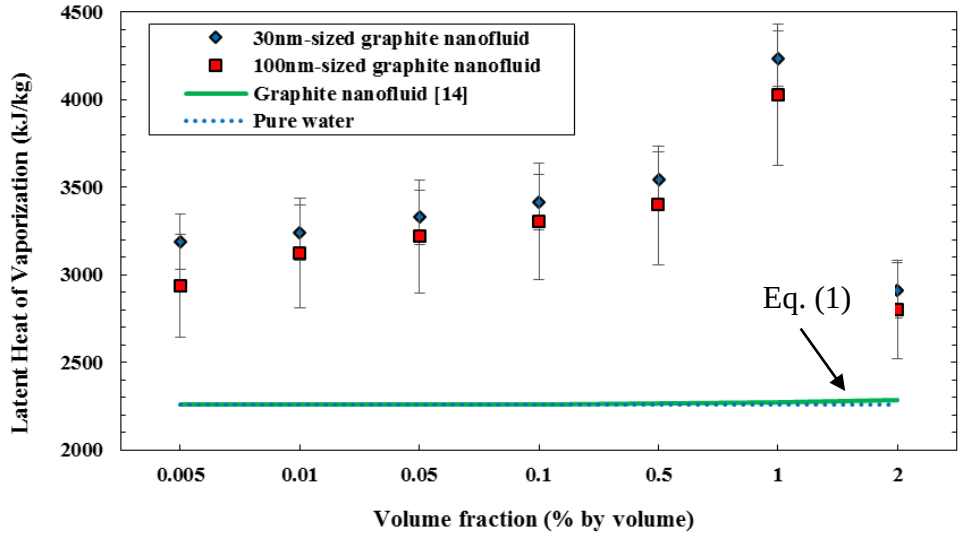

(b)

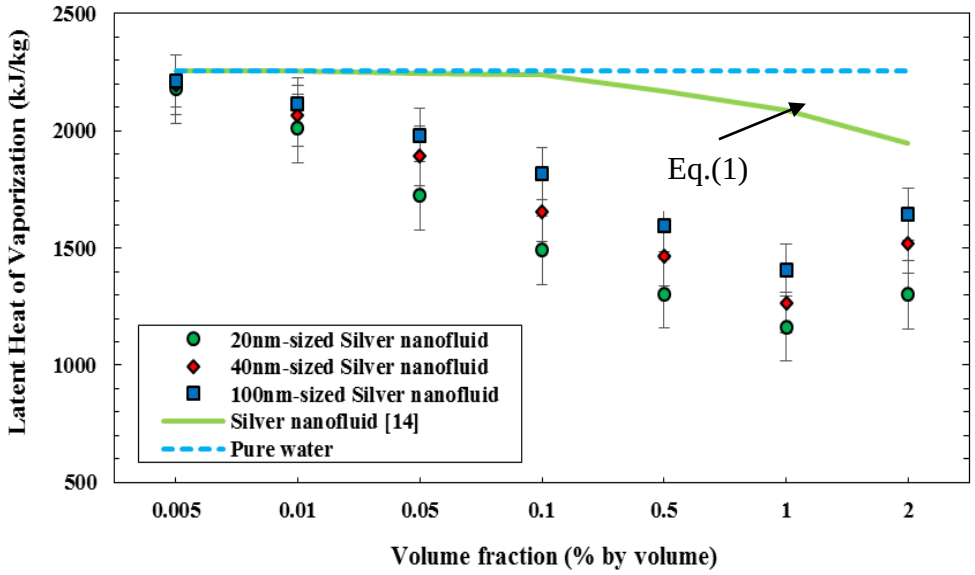

Figure 12 (a) Measured Latent Heat of Vaporization in Graphite Nanofluids and (b) in Silver Nanofluids (the Trends are Changed after 1% Volume Fraction), Including Calculated Latent Heat of Vaporization in Graphite and Silver Nanofluid Using Eq. (1) based on Changes in the Volume Fraction **[14]**.

Based on these limited data, the size of the nanoparticles has a small effect on h_{fg}, with smaller-sized nanoparticles apparently causing a slightly greater change in h_{fg} relative to that for pure water. Similarly for silver nanofluids (Fig. 12(b)), h_{fg} decreases with increasing volume fraction up to 1%, with smaller nanoparticles causing a greater change in h_{fg}. The change in behavior at 1% volume fraction is discussed further below with respect to the total surface area of the nanoparticles.

The calculated h_{fg} in aqueous graphite and silver nanofluids using Eq. (1) with volume fraction changes is in Figs. 12(a) and 3(b). From Eq. (1) with water density (0.9584 g cm^{-3}), silver density (10.49 g cm^{-3}), graphite density (2.23 g cm^{-3}), water boiling temperature (373.15 K), silver boiling temperature (2435 K), graphite boiling temperature (5800 K), pure water h_{fg} (2257 kJ kg^{-1}), pure silver h_{fg} (2356 kJ kg^{-1}), and pure graphite h_{fg} (29650 kJ kg^{-1}), the h_{fg} of silver nanofluid and graphite nanofluid can be obtained.

That is, h_{fg} of aqueous graphite nanofluid increased and h_{fg} of silver nanofluid decreased as the volume fraction increases. The results indicate similar qualitative trends as the experimental results in Figs. 12 (a) and 12 (b). However, these theoretical results are limited, since they neglect other properties (i.e. surface tension and viscosity) and physical phenomena (agglomeration and effective volume fraction change). A model which incorporates these would be able to predict h_{fg} more accurately, and will be discussed in Chapter 3.

With the exception of volume fractions greater than 1%, the results in Fig. 12 show that size and volume fraction are both important, which leads to the hypothesis that surface area is a key parameter for the observed changes in h_{fg}. Accordingly, the change in h_{fg} relative to that for pure water (with surfactant) is plotted as a function of total nanoparticle

surface area in Fig. 13. In Fig. 13, h_{fg} of graphite nanofluids increases as the surface area of nanoparticles increases, and h_{fg} of silver nanofluids decreases as the surface area of nanoparticles increases, except for the points representing a volume fraction of 2%. That is, Fig. 13 indicates the same trend for both graphite and silver nanofluids, increasing the absolute value of the h_{fg} difference with increasing surface area up to that corresponding to a 1% volume fraction.

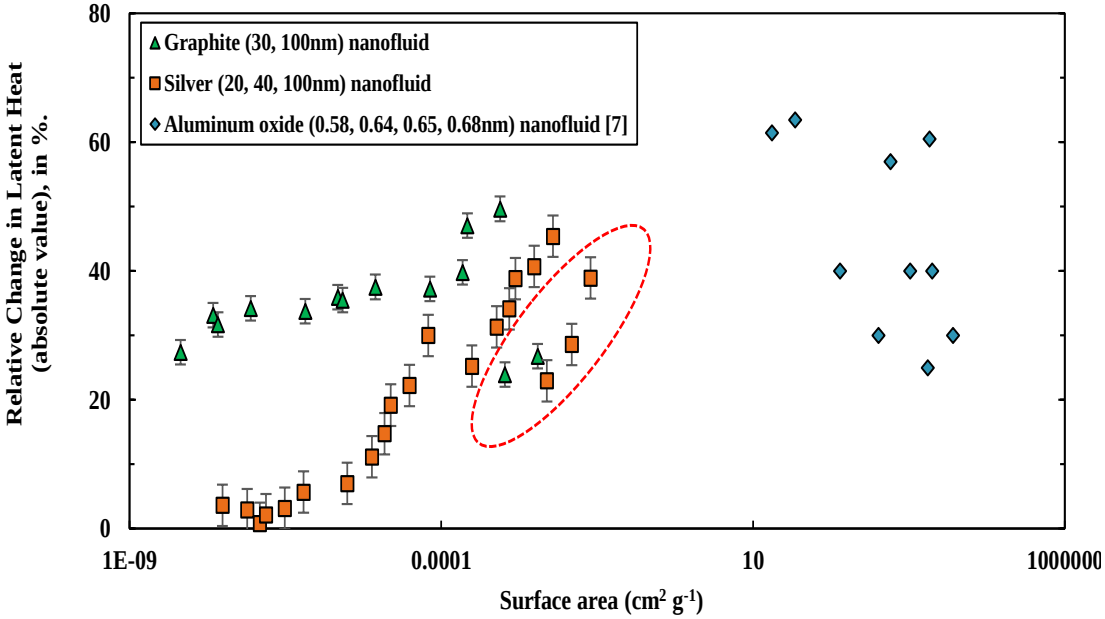

Figure 13. Absolute Values of the Increased h_{fg} for Graphite and Aluminum Oxide Nanofluids **[7]** and the Decreased h_{fg} of Silver Nanofluids relative to that for Pure Water with Surfactant (2132 kJ kg-1) (%) **[7]** in terms of Surface Area Changes, Compared with Ameen's Results for Aluminum Oxide Nanoparticles **[7]**. That is, the Relative Change in h_{fg} Increases with Increasing Surface Area. The Trends Change at the Circled Points near 2% Volume Fraction for Silver and Graphite Nanofluids because of Agglomeration.

This suggests that these phenomena (increased and decreased h_{fg}) are possibly caused by the number of interactions between nanoparticles and water molecules. Increased h_{fg} in graphite nanofluid can potentially be explained by additional interactions between graphite nanoparticles and water molecules. However, decreased h_{fg} in the silver nanofluid could be related to the surface melting of silver nanoparticles in water because it prevents interactions between water molecules and silver nanoparticles, as is indicated by a Hamaker constant calculation shown later in Chapter 4 [28]. As a result, the broken hydrogen bonds could not be replaced due to the surface melting, and a decrease in h_{fg} could also be realized.

However, as shown in Figs. 12(a) and 12(b), 2% volume fractions of graphite and silver nanofluids indicate that the h_{fg} of the nanofluids suddenly approach the standard h_{fg} of pure water even though the surface area of the nanofluids increases as is shown in Fig. 13. This is explained by the fact that agglomeration substantially increased at volume fractions around 2%. Particle size (indicating the extent of agglomeration) was observed before and after heating by a Dynamic Light Scattering instrument (DLS, Nicomp 380 ZLS). As shown in Figs. 14 (a) and 14 (b), graphite nanoparticles were highly agglomerated during the heating process, from 48nm ± 2nm to 178 ± 2nm, and the silver nanoparticles in water also changed their size from 27nm ± 2nm to 90nm ± 2nm after heating.

According to this measurement, the surface area of silver and graphite nanoparticles is reduced due to the agglomeration. Therefore, the trend in h_{fg} for graphite and silver nanofluids changes direction and returns to the standard h_{fg} of water beyond 1% volume fraction. Motivated by this experimental evidence, all the results was plotted together in Fig. 13 to determine if surface area was the key parameter. As the surface area of the

nanoparticles increases, the latent heat change also increases. In other words, the variation of h_{fg} in silver and graphite nanofluids depends on the surface area, when the agglomeration rate is not significant. Although surface area appears to be the most important parameter, there are several underlying phnenomena that can change the surface area which could be explored.

As mentioned in this chapter, nanoscale effects such as possible surface melting of silver nanoparticles that hinders the interactions between water molecules and silver nanoparticles and hydrophobic interactions of graphite nanoparticles in pure water that intensify the interactions between water molecules and graphite nanoparticles could also be of importance [10] [19] [28] [29] [30] [31] [32]. These nanoscale phenomena could answer the question why small amounts of nanoparticles can substantially vary the latent heat of vaporization in water. These will be presented in Chapter 4.

(a)

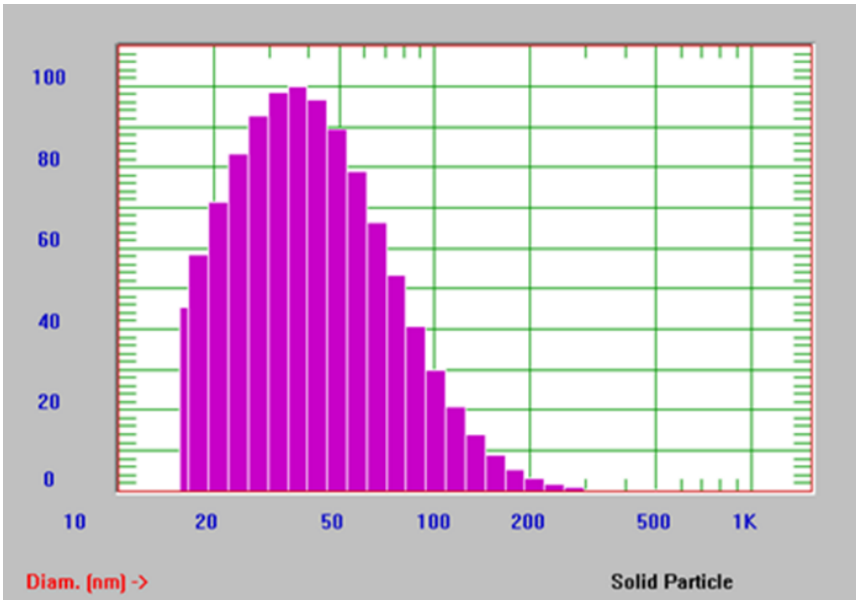
100
80
60
40
20
0
10
20
50
100
200
500
1K
Diam. (nm) ->
Solid Particle

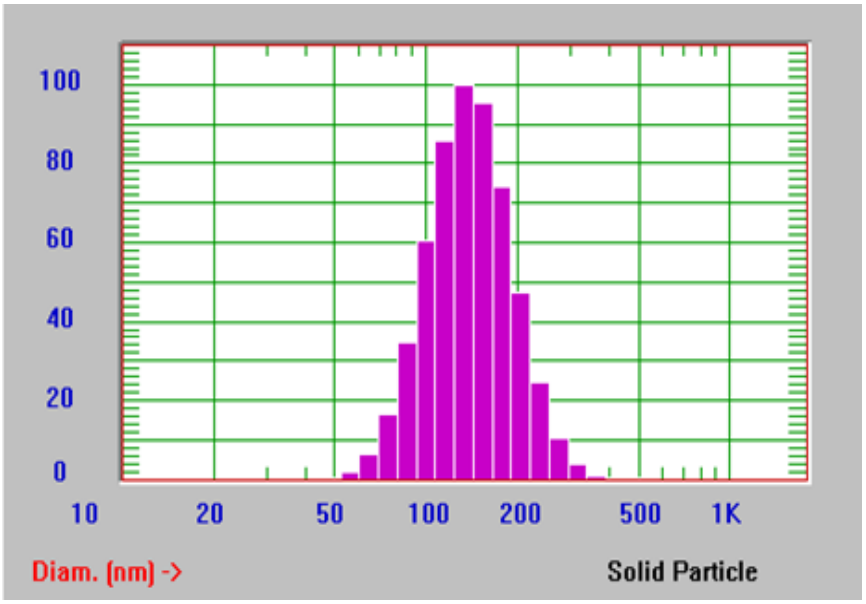
100
80
60
40
20
0
10
20
50
100
200
500
1K
Diam. (nm) ->
Solid Particle

(b)

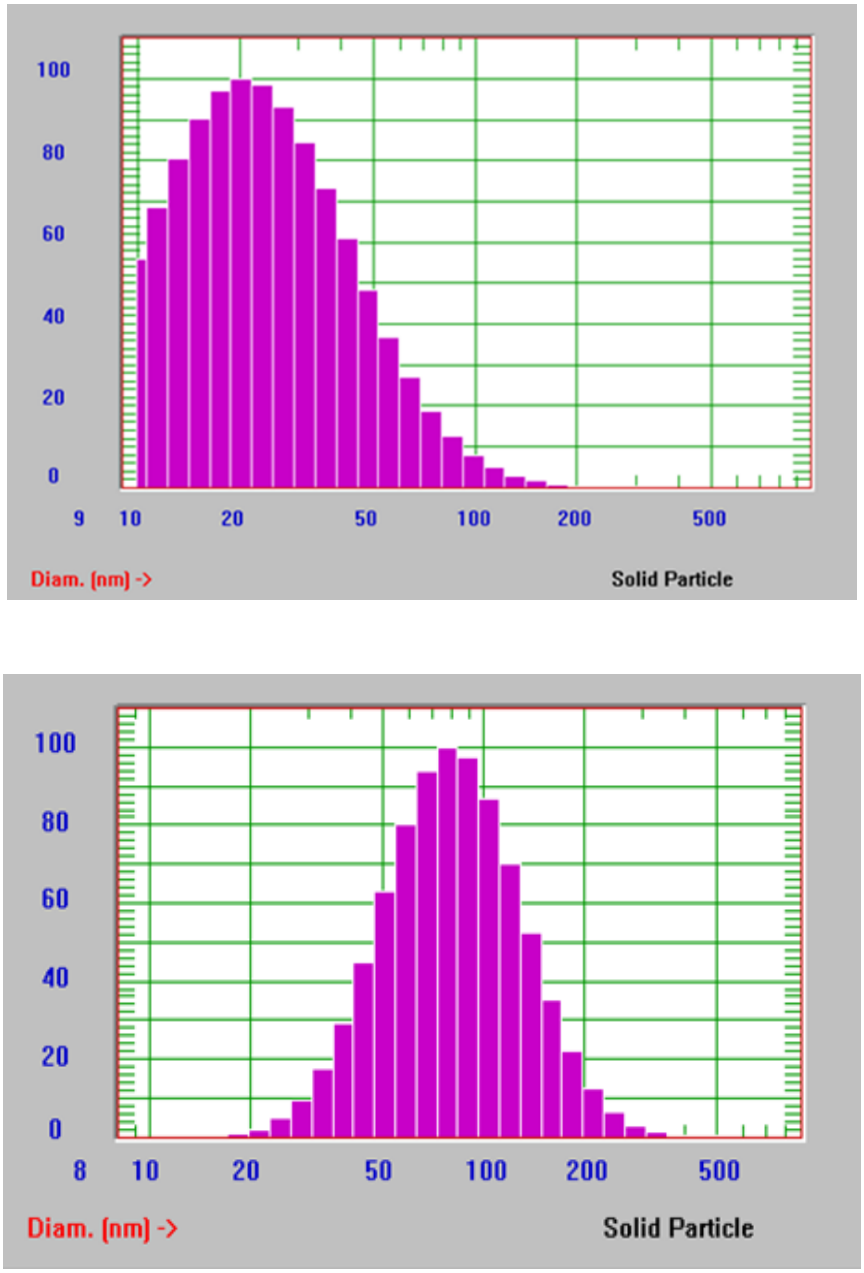

Figure 14 Average Size Change of 2% Volume Fraction, 30-nm (a) Graphite Nanofluid before Heating (48 ± 2nm, upper) and (178 ± 2nm, lower) after Heating, and (b) 2% Volume Fraction, 20-nm Silver Nanofluids (27nm ± 2nm, upper) before Heating and after Heating (90nm ± 2nm, lower)

2.4 Summary

In this dissertation, recent literature has proposed that the h_{fg} in nanofluids is increased due to the additional (volumetric) interactions between nanoparticles and water molecules. The new results reported here indicate that h_{fg} in graphite nanofluid can be substantially increased, while h_{fg} in silver nanofluid can be substantially decreased. In addition, h_{fg} with the changing surface area in terms of the volume fractions and the size of the nanoparticles is investigated. As a result, the increased and decreased h_{fg} in graphite and silver nanofluids are highly related to the surface area and can be controlled by the surface area due to the interactions between nanoparticles and water molecules. If agglomeration can be avoided, then greater than 40% changes in h_{fg} are possible. However, it is not clear that this holds above the small volumes tested at the lab scale, i.e., it is not yet clear if the h_{fg} results can be applied to real-world applications such as solar steam generators and latent thermal storage systems. Moreover, further study about nanoscale phenomena is provided in Chapter 4 to investigate details of the decreased and increased h_{fg}, and attempt to explain these observations.

CHAPTER 3. MEASUREMENT OF THERMOPHYSICAL PROPERTIES FOR LATENT HEAT OF VAPORIZATION IN AQUEOUS SILVER AND GRAPHITE NANOFLUIDS

Experimental results of h_{fg} in Chapter 2 indicate that by adding nanoparticles, it is possible to significantly change h_{fg} [10]. In addition, as discussed in Chapter 1, Ameen et al. [7] reported the enhancement of h_{fg} in Pt nanofluid using molecular dynamics (MD) simulation. However, based on their approaches, the considerable variation in h_{fg} of silver and graphite nanofluids up to ± 30% could not be explained by the MD simulation. Therefore, theoretical analysis for h_{fg} is required to support the experimental results. In this section, a conceptual analysis of h_{fg} for aqueous nanofluids based on the modified Clausius-Clapeyron equation is employed with the measured thermophysical properties, i.e., density and surface tension. This approach can be used for developing improved understanding about how h_{fg} in silver and graphite nanofluids is altered.

3.1 Clausius-Clapeyron Equation for h_{fg}

To explain the variation of h_{fg} theoretically, the Calusius - Clapeyron equation is required. To begin with, the Clausius-Clapeyron equation is derived from the Maxwell equation, which can be expressed by [33]:

$$\left(\frac{\partial S}{\partial v}\right)_T = \left(\frac{\partial P}{\partial T}\right)_v \tag{8}$$

where S is the entropy, v the specific volume, T the temperature, and P the pressure. During a phase change from liquid to vapor, the pressure can be considered as a constant, the saturation pressure [33]. Since the pressure is dependent on the temperature and independent of the specific volume, the partial derivative $\left(\frac{\partial P}{\partial T}\right)$ is treated as a total derivative $\left(\frac{dP}{dT}\right)$ and based on a P-T diagram, the specific volume can be considered as a constant. Thus, for an isothermal liquid-vapor phase change process, an integration yields:

$$\int_f^g dS = \int_f^g \left(\frac{\partial P}{\partial T}\right)_v dv$$

$$S_g - S_f = \left(\frac{dP}{dT}\right)_{sat} (v_g - v_f) \tag{9}$$

where g is saturated vapor, f saturated liquid, and sat the saturation condition. In order to derive h_{fg} with the Maxwell equation , the enthalpy relation is also required, and it is given as:

$$h_{fg} = TS_{fg} \tag{10}$$

At the phase change at constant temperature and pressure, the two phases are in equilibrium, and the Gibbs free energy equals to zero. Therefore, the Gibbs free energy equation, $G_{fg} = h_{fg} - TS_{fg}$, is modified as Eq. (10) [19]. Based on Eqs (9) and (10), the Clausius-Clapeyron equation for h_{fg} is derived and can be represented as:

$$h_{fg} = Tv_{fg}\left(\frac{dP}{dT}\right)_{sat} \tag{11}$$

In Eq. (11), the specific volume, v_{fg}, can be substituted by the density, $(\rho_f - \rho_g)/(\rho_f \rho_g)$. In addition, the surface tension is given by [34] :

$$\sigma^{\frac{1}{4}} = \frac{[P](\rho_f - \rho_g)}{M} \tag{12}$$

where M is molar mass, [P] the parachor, σ the surface tension, and ρ the density. The surface tension can replace $(\rho_f - \rho_g)$ based on Eq. (12). Therefore, finally, substituting v_{fg} with $(\rho_f - \rho_g)/(\rho_f \rho_g)$ with Eq. (11) and modifying Eq. (11) with Eq. (12) provides a method to determine h_{fg} by measuring surface tension and density:

$$h_{fg} = \frac{TM\sigma^{\frac{1}{4}}}{[P]\rho_f \rho_g}\left(\frac{dP}{dT}\right)_{sat} \tag{13}$$

The parachor can be derived from an empirical constant depending on the value of the surface tension, density, and molecular mass before heating – i.e., at room temperature [note: ρ_g is neglected because it is too small, compared to ρ_f]

$$[P] = \frac{\sigma^{\frac{1}{4}} M}{\rho_f} \tag{14}$$

The parachor is independent on temperature, thus it can be considered as a constant for h_{fg} calculation. Based on the experimental measurements, the boiling temperature and the saturated pressure are identical for the fluids, therefore, the standard values of pure water are used to derive h_{fg} in nanofluids using Eq. (13). The molecular mass is calculated based on the volume fraction of pure water, nanoparticles, and a surfactant [35]. Also, the density of fluids is measured by a simple method, which is dividing mass by volume using a graduated cylinder and a sensitive balance (Mettler Toledo, AB265S, 0.01mg accuracy) while conducting the experiments at room temperature. The density of nanofluid can be calculated by the volume fraction and the density of nanoparticles, and the density of the base fluid [4] [36]. However, the non uniform heat distribution in the test sample due to the locally heated nanoparticles by the volumetric heat source is difficult to be considered in the calculation because the present model of density cannot be well matched with the experimental results as temperature increases [36]. Therefore, in this dissertation, the density of nanofluids is determined by experiments. Since the density of the fluids is highly related to the strength of interactions, i.e., water-water interactions, water-nanoparticle interations, the measured density of each fluid in Table 10 indicates the different values.

That is, it is possible to conclude that the interations in aqueous nanofluids could be changed while conducting the experiments.

In addition, based on Eq. (13), the surface tension is also an important factor to determine h_{fg} in fluids, since temperature, molecular mass, parachor constant, gas density and pressure were considered as constant while boiling. Therefore, the surface tension of aqueous silver, graphite nanofluids, and pure water was measured by a tensiometer (Kruss K100), and the values are shown in Fig. 15. The uncertainty of these measurements was calculated by five trials and the averaged surface tension results. The results were validated by comparing the standard value with experimental results of pure water without SDS. The extrapolated surface tension of pure water without SDS based on the measurements is 59.68 mN m^{-1}. It is close to the standard value (58.8 mN m^{-1}) at 100 °C of pure water without SDS. Therefore, the results in Table 9 from the fluids can be trusted. However, in Fig. 16, the surface tension values for pure water without SDS are not included because the values of pure water without SDS are much greater than other fluids. Therefore, it is difficult to compare the results of all fluids.

(a)

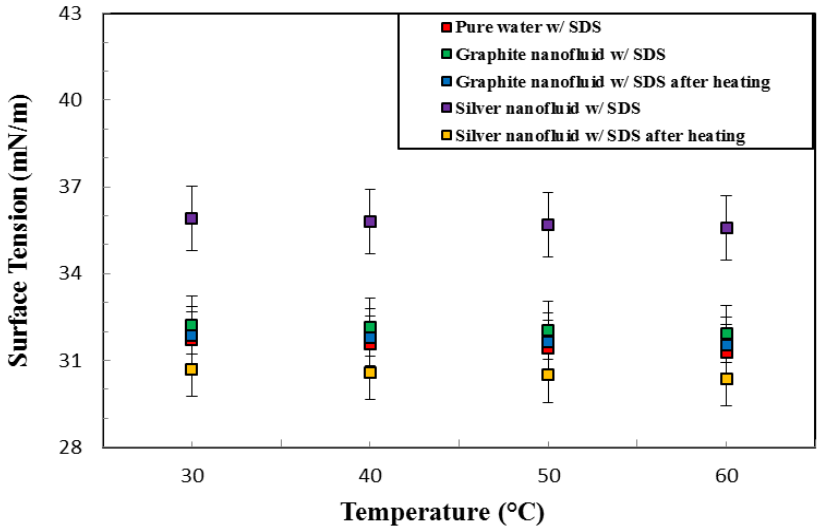

(b)

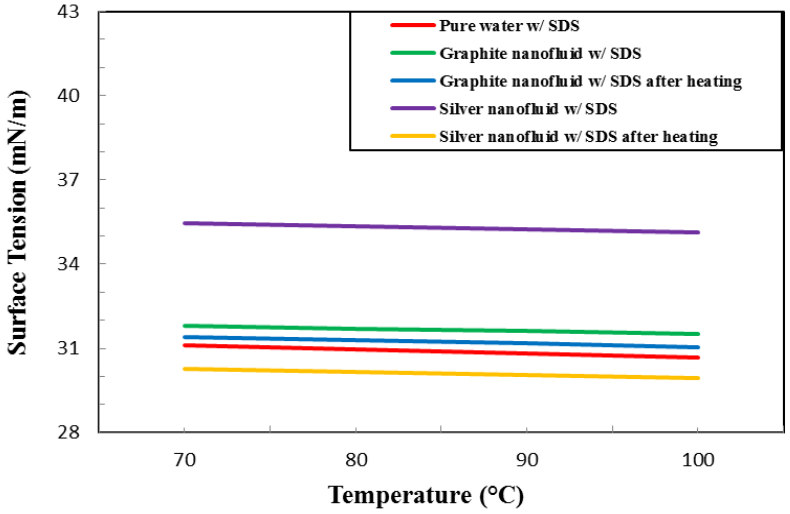

Figure 15. The Surface Tension Changes in Nanofluids with 1% Surfactant as a Function of the Temperature (a) the Measured Surface Tension from 30°C to 60°C, and (b) the Values between 70°C and 100°C were Extrapolated based on the Results from 30°C to 60°C due to the Temperature Limitations of the Tensiometer.

Table 9 The Measured (Averaged) and Extrapolated Surface Tension Results of Fluids

	Pure water (w/o SDS)	Pure water (w/ SDS)	Graphite nanofluid (w/ SDS)	Heated Graphite nanofluid (w/ SDS)	Ag nanofluid (w/ SDS)	Heated Ag nanofluid (w/SDS)
30 °C	65.61	31.71	32.23	31.87	35.91	30.69
40 °C	64.74	31.57	32.14	31.79	35.79	30.58
50 °C	63.91	31.42	32.04	31.65	35.69	30.49
60 °C	63.07	31.27	31.92	31.52	35.58	30.37
70 °C*	62.22	31.12	31.82	31.40	35.47	30.26
80 °C*	61.38	30.98	31.71	31.29	35.36	30.16
90 °C*	60.53	30.83	31.61	31.17	35.25	30.05
100 °C*	59.68	30.68	31.51	31.05	35.14	29.94

* Indicate the extrapolated results based on the measured values from 30°C to 60°C.

3.2 Theoretical Results and Discussion

As a result, the theoretical results with the measured parameters in Table 10 indicate the same trends as the experimental results for h_{fg} in nanofluids. Table 10 shows the calculated h_{fg} values in nanofluids using Eq. (13) along with the measured surface tension,

densities, and corresponding parachor while conducting the experiments. The calculated molar mass is also added in Table 10.

Table 10 The Theoretical Results of h_{fg} in Nanofluids and Pure Water with Surfactant, Based on Eq. (13)

	Pure water (w/ SDS)	Silver/water nanofluid (w/ SDS)	Graphite/water nanofluid (w/ SDS)
Surface tension (σ) [mN/m]	30.68	29.94	31.05
Molecular mass (M) [g/mol]	20.90	21.01	20.92
Density of liquid (ρ_f) [g/cm^3]	0.9713 ± 0.09	1.1086 ± 0.12	0.8901 ± 0.08
Density of vapor (ρ_g) [g/cm^3]	0.000598	0.000598	0.000598
Parachor ([P])	50.31	50.92	50.42
Latent heat of vaporization (h_{fg}) [kJ/kg]	2279	1972	2467
Measured latent heat of vaporization (h_{fg}) [kJ/kg]	2132	1492	3341

Since the standard Parachor value for pure water is 51 [35], the measured Parachor value (52.7) for pure water without SDS using Eq. (14) is reliable. Based on the results in Table 10, there exists a 25% difference in h_{fg} between the theoretical and the experimental results. Therefore, nanoscale interactions between nanoparticles and water molecules

should be investigated. Therefore, Chapter 4 discusses nanoscale studies about the presence of melted silver nanoparticles in water by volumetric heating and hydrophobic interactions by graphite nanoparticles.

CHAPTER 4. NANOSCALE STUDIES FOR LATENT HEAT OF VAPORIZATION IN AQUEOUS NANOFLUIDS

From Chapter 3, the surface tension and the density of nanofluids are different than the comparable properties of pure water. Therefore, it is possible that placing the nanoparticles in water could affect other thermophysical properties as well. That is, from the enthalpy relation in Eq. (10), the entropy change, which is related to the surface tension and the density is an important factor for increased or decreased h_{fg} because the boiling temperature and vapor entropy are the same for an aqueous nanofluid as for pure water. For example, the variation of h_{fg} in pure water can be calculated by Eq. (10). For pure water, h_{fg} (2257 kJ kg^{-1}) can be obtained by the boiling temperature (373.15 K), the entropy of the saturated vapor (7.3549 KJ kg^{-1} K^{-1}) and the entropy of the saturated liquid (1.3669 KJ kg^{-1} K^{-1}) [33]. Since the boiling point in aqueous nanofluids (confirmed by thermocouple measurements) and the entropy of the saturated vapor are not changed compared to pure water, h_{fg} in aqueous nanofluids could be determined by the entropy of the saturated liquid. Therefore, the entropy change of the liquid nanoparticle suspension due to the nanoscale interactions should be investigated to confirm the h_{fg} variations. The following sections therefore discuss the entropy change of aqueous nanofluids based on repulsion between water molecules and nanoparticles caused by melting of silver nanoparticles using a Hamaker constant calculation, and hydrophobic interactions of graphite nanoparticles, since these could be primary reasons for increased or decreased entropy compared to the value for pure water.

4.1 Low Temperature Melting of Silver Nanoparticles in Subcooled and Saturated Pure Water

Only a few papers conclude that h_{fg} in nanofluids is increased due to the additional interactions between nanoparticles and water molecules [7] [11] [12]. However, in Chapter 2 of this dissertation results are presented that h_{fg} in aqueous silver nanofluid could be decreased when heated by a volumetric heat source, i.e., a 130-mW laser. To investigate the reason, first a series of evaporation experiments with silver nanofluid, graphite nanofluid, and pure water was conducted. The remaining fluid level for all fluids was recorded every day and the fluid level after 30 days in a fume hood with the exact same conditions, i.e., temperature, humidity, and pressure, showed the different results as presented in Fig. 16. These results indicate that the evaporation rate of graphite and silver nanofluids is much slower than that for pure water because surface forces of the nanofluids are higher than that of pure water. That is, at room temperature, adding nanoparticles in water can always increase interaction forces.

Also, low power input (80mW, less than the laser power output (130mW)) experiments in silver nanofluid using a power supply and hot wire in Fig. 8 were conducted to investigate whether a relatively low temperature (130 °C) immersed hot wire could affect the decreased h_{fg} in aqueous silver nanofluid. This experiment led to a measured h_{fg} in aqueous silver nanofluid of 2536 kJ kg^{-1}, i.e., *greater* than that for pure water (2267 kJ kg^{-1}) [10]. In other words, reducing the temperature of the heat source reversed the change in h_{fg}.

(a)

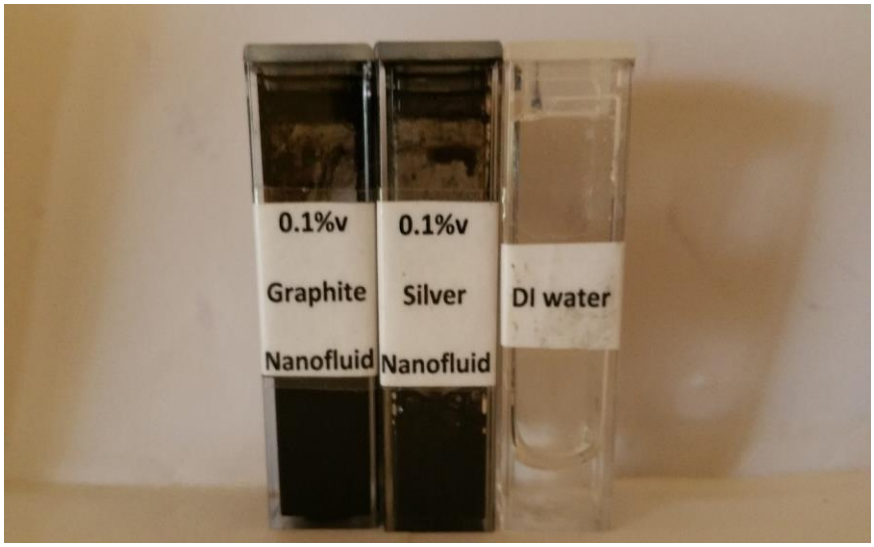

(b)

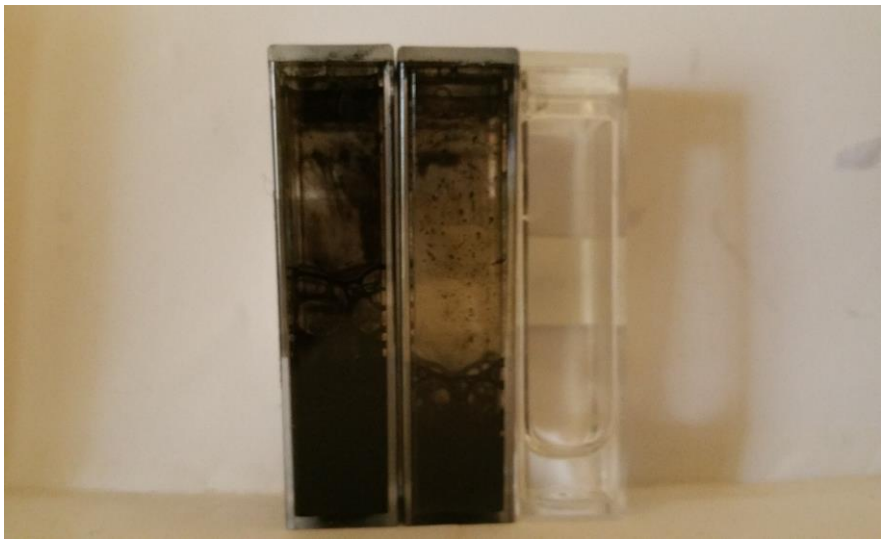

Figure 16. Fluid Level Changes due to the Evaporation Rate Difference for Graphite Nanofluid with SDS, Silver Nanofluid with SDS, and Pure Water (a) Front Sides, and (b) Back Sides (from the left: Graphite Nanofluid, Silver Nanfluid, and Water)

Based on the evaporation rate, which is also related to the interaction forces between water molecules or nanoparticles and water molecules [19] and low power input experiments, melting of silver particles in water caused by relatively high temperatures could be a possible reason for the decreased h_{fg} in aqueous silver nanofluid. Compared to bulk metal, metallic nanoparticles have been shown to have a significantly lower melting temperature as depicted in Fig. 17 [29] [31] [37]. Melting of metallic nanoparticles when placed in de-ionized (DI) water has not yet been adequately studied or explained due to the difficulty of predicting and observing the melting behavior of particles in a solution [38].

In this dissertation, the melting-based temperature dependence of the Hamaker constant values in a (10nm, 20nm, and 100nm) silver nanofluid to investigate the interaction between interfaces (silver-melt-water) is calculated. In addition, Transmission Electron Microscopy (TEM) and Dynamic Light Scattering (DLS) is performed to show that the average size of silver nanoparticles/aggregates is reduced after light-induced heating. Taken together, these indicate that it is possible to melt silver nanoparticles (which have a bulk melting point of 961˚C) while suspended in water of < 100˚C with relatively low power inputs (130mW).

4.1.1 Surface Melting of Silver Nanoparticles in Water

Three hypotheses, based on the literature, are employed in this chapter: homogeneous melting (HM), liquid nucleation and growth (LNG), and liquid skin melting (LSM).

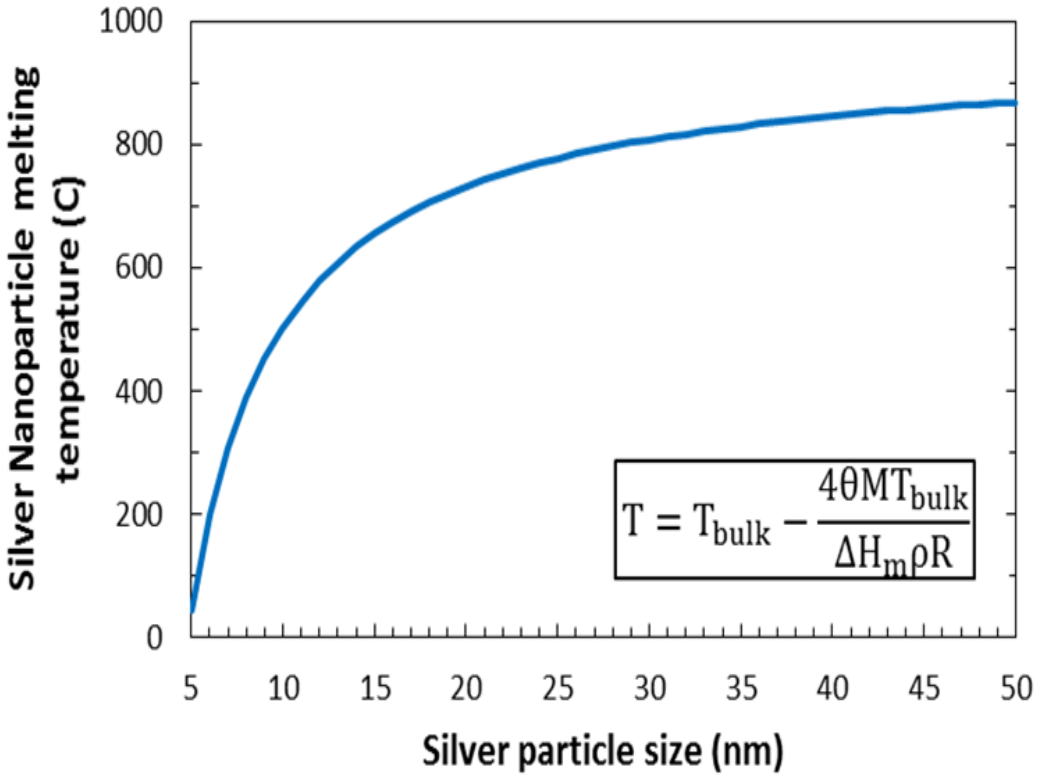

Figure 17. Size-Dependent Melting Temperature (°C) Change based on the Gibbs-Thomson Equation **[30] [31]**, where T is the Temperature of the Nanoparticle, T_{bulk} the Melting Temperature of Bulk Ag, θ Surface Energy, M Atomic Mass, ΔH_m Melting Enthalpy, ρ Density, and R the Diameter of the Nanoparticles **[31]**.

(a)

(b)

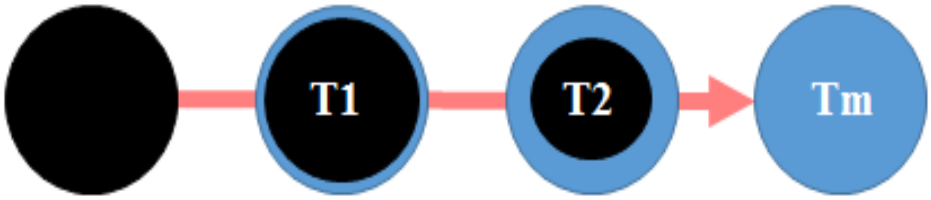

(c)

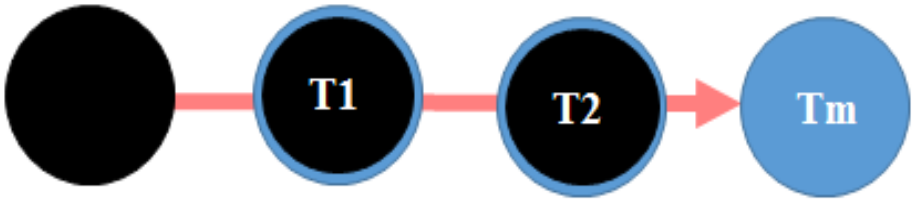

Figure 18. Three Hypotheses for the Melting of Nanoparticles Suspended in a Solution: (a) Homogeneous Melting (HM) (b) Liquid Nucleation and Growth (LNG) (c) Liquid Skin Melting (LSM)

HM is that the entire solid is in equilibrium with the entire melted particles without surface melting, LNG is the process that a liquid layer nucleates and grows with temperature, and LSM considers the formation of a liquid layer over the solid core at a low temperature that remains unchanged until the solid particle transforms completely to liquid at the melting temperature [37]. All three have been suggested for the melting of nanoparticles [37] and are described in Fig. 18. To support these hypotheses, researchers have conducted in-situ experiments using a conduction-based heat input with TEM over a certain time period in order to identify the melting of metallic nanoparticles [29] [31] [32] [37]. The results indicate that there is decreased diameter of 8nm-sized silver nanoparticles after 740s as temperature is increased up to 627 ^{0}C [32]. Therefore, liquid skin melting (LSM), which is surface melting of nanoparticles, could occur during the heating. In other words, surface melting of metallic nanoparticles in a fluid could possibly be realized during high temperature heating since thermophoresis would tend to move particles out of the heated region of the sample before the entire nanoparticle melts.

4.1.2 Hamaker Constant for Surface Melting-Based Aqueous Nanofluid

In order to experimentally investigate the melting of silver nanoparticles by light (volumetric) absorption, near-field phenomena have to be considered, such as the interactions between silver nanoparticles and the water molecules. Therefore, to investigate dispersion forces, which are Van der Waals (VdW) interaction forces between interfaces, a size-dependent Hamaker constant can be determined [39] [40]. The Hamaker constant is useful since it accurately quantifies the interactions of particles. The Hamaker constant is

defined for a Van der Waals two-body potential [39] [40]. A large value of the Hamaker contant means strong Van der Waals two-body forces compared to a smaller value [19]. Positive Hamaker constant describes that two bodies is attractive, whereas negative Hamaker constant can be repulsive between two particles [19]. The size-dependent Hamaker constant of silver nanoparticles in water or vacuum can be found based on the Lifshitz theory, which calculate the forces in terms of dielectric constants of materials and refractive incices [39]. Also, during melting, three phases will be present (solid-melt-vapor), which can be calculated for metals and semiconductors [41]. Even though melting of silver nanofluids has been studied, a temperature-dependent Hamaker constant which considers the influence of the melting in ambient pressure, subcooled, and saturated water-based silver nanofluids has not yet been determined [17] [42]. Thus, it is proposed herein that a non-retarded Hamaker constant ('non-retarded' is explained below) can be used to predict melting for silver nanofluids with respect to near-field surface melting of silver nanoparticles in water. The fundamental phenomena of this process are described in Fig. 19 (a), where ε_1 represents a silver nanoparticle with a range of sizes (diameters of 10nm, 20nm, and 100nm), ε_2 is water, and ε_3 is melted (liquid) silver. Dispersion forces between various-sized silver nanoparticles and water can be approximated as two parallel plates separated by the thickness of the melted silver layer, as shown in Fig. 19 (b) [39]. The Van der Walls force is effective only up to several hundred angstroms. This is called the *non-retarded* regime, and when the interaction is far apart, the force decays faster than $1/r^6$ (r is the distance between two bodies). This is called the *retarded* regime [19] [43]. Thus, in

(a) **(b)**

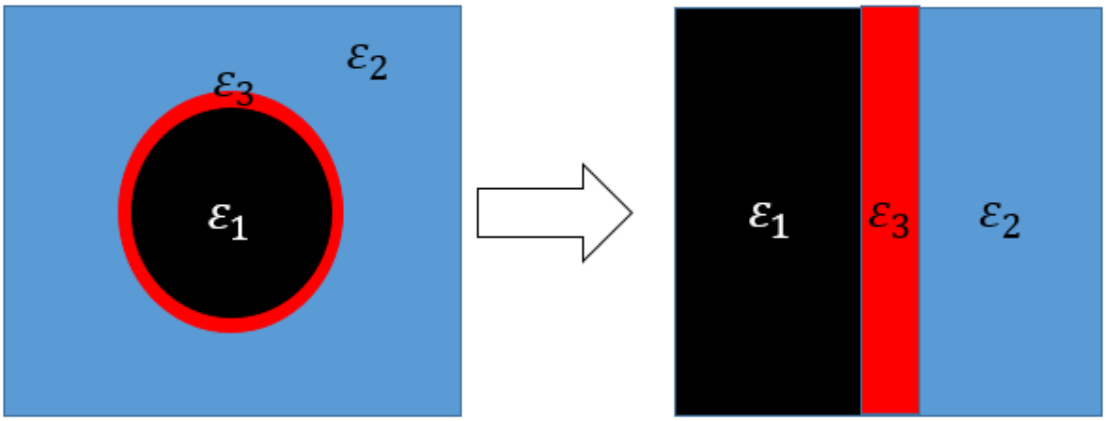

Figure 19. Modeled Geometry of Surface Melting of Silver Nanoparticles in Water [39]

this dissertation, the non-retarded Hamaker constant A_{132} is calculated and can be described by [19] [39] [43]:

$$A_{132} = \frac{3}{4\pi}\hbar w_{132} \tag{15}$$

where $\hbar$ is the Planck constant, and w_{132} the Lifshitz constant defined as [19] [32] [43]:

$$w_{132} = \int_0^{\infty} \left(\frac{\varepsilon_1(i\omega) - \varepsilon_3(i\omega)}{\varepsilon_1(i\omega) + \varepsilon_3(i\omega)}\right)\left(\frac{\varepsilon_2(i\omega) - \varepsilon_3(i\omega)}{\varepsilon_2(i\omega) + \varepsilon_3(i\omega)}\right) d\omega \tag{16}$$

where ε_n (iω) is the permittivity of the nth medium as a function of the imaginary frequency iω [39] [41]. The Lifshitz constant is the theory relating the Hamaker constant to dielectric constants of the materials [19]. The imaginary frequency iω is given by:

$$\varepsilon_n(\mathrm{i}\omega) = 1 + \frac{2}{\pi}\int_0^{\infty}\left(\frac{x\, Im\varepsilon_n(x)}{x^2+\omega^2}\right)dx \tag{17}$$

For example, a charge in the medium interacts with a surface of the other medium (an image charge). Therefore, the imaginary frequency should be considered in the permittivity calculation to calculate the interaction forces [19]. In order to obtain the size dependence of the Hamaker constant [39], the size-dependent dielectric permittivity is required. The size-dependent dielectric permittivity can be obtained from the size-modified Drude permittivity [19] [32] [41]. Therefore, the size-modified dielectric permittivity of silver nanoparticles is defined as [39] [44]

$$\varepsilon(\omega, \mathrm{R}) = \varepsilon_{bulk,Ag}(\omega) + \omega_P^2\left(\frac{1}{\omega^2+\gamma_\infty^2} - \frac{1}{\omega^2+\gamma(R)^2}\right) + i\frac{\omega_P^2}{\omega}\left(\frac{\gamma(R)}{\omega^2+\gamma(R)^2} - \frac{\gamma_\infty}{\omega^2+\gamma_\infty^2}\right) \tag{18}$$

where R is the radius of a silver nanoparticle, ω_P the plasma frequency, γ the electron scattering rate, and $\gamma(R)$ the modified scattering rate of metal. This is given as [39] [44]:

$$\gamma(R) = \gamma + \mathrm{A}\,\frac{v_F}{R} \tag{19}$$

where A is a dimensionless constant of the order of 1, which is convenient to write the scattering rate of metal [43] and v_F is the Fermi velocity [39] [44]. Frequency-dependent optical property data for subcooled water (25°C) is available up to 9.4 x 10^{15} Hz (wavelengths of 200nm - 200μm), which includes the visible range of light [39] [45] [46]. However, such data for saturated water (100°C) are limited to a small region of wavelengths (0.2μm - 2μm), thus a reliable Hamaker constant for saturated water could not be obtained [47]. Therefore, in this dissertation, only subcooled water is considered in the calculation of the temperature-dependent Hamaker constant of aqueous silver nanofluid. Moreover, experiments to measure the optical properties at high temperature for solid and liquid silver have rarely been conducted [47]. Therefore, a temperature-dependent Drude model is used to determine the dielectric permittivity - i.e. $\varepsilon_{bulk,Ag}(\omega)$ in Eq. (22) of solid nanoparticles and molten silver [48] [49] [50]:

$$\varepsilon_{bulk,Ag}(\omega) = \varepsilon_1(\omega) - i\varepsilon_2(\omega) \tag{20}$$

$$\varepsilon_1(\omega) = 1 - \frac{\sigma_0\tau}{\varepsilon_0}\frac{1}{[1 + (\omega\tau)^2]} \tag{21}$$

$$\varepsilon_2(\omega) = \frac{\sigma_0}{\varepsilon_0 \omega} \frac{1}{[1 + (\omega\tau)^2]} \tag{22}$$

where σ_0 is the electrical conductivity, ε_0 the vacuum permittivity, and τ the collision time for electrons [48] [49] [50]:

$$\tau = \frac{\sigma_0 m_e}{n_e e^2} \tag{23}$$

where σ_0 is the electrical conductivity, m_e the effective electron mass, n_e the electron density, and e the electron constant. The electron density is defined as [48] [49] [50]:

$$n_e = N_{val} \frac{\rho}{u} \tag{24}$$

where N_{val} is the number of electrons in the valence band, ρ the mass density of the silver, and u the molecular weight of the silver. The parameters for Eqs. (15)-(24) are taken from the literature, and are given in Table 11 [39] [48] [49] [50] [51].

Table 11 Parameters for the Calculation of the Temperature-Dependent Dielectric Permittivity of Solid and Liquid Silver (Melting Temperature is Calculated Based on the Eq. in Fig. 16.

Parameter	Description	Value
$\boldsymbol{\omega_P}$	Plasma frequency	$5.08 \times 10^{15}\ s^{-1}$
$\boldsymbol{\gamma}$	Electron scattering rate	$0.01\omega_P$
$\boldsymbol{v_F}$	Fermi velocity	$1.39 \times 10^{6}\ ms^{-1}$
$\boldsymbol{\sigma_0}$	Electrical conductivity of silver	$2.04 \times 10^{7}\ Sm^{-1}$ at melting point of 10nm diameter size (~527 ˚C) $1.56 \times 10^{7}\ Sm^{-1}$ at melting point of 20nm diameter size (~727 ˚C) $1.24 \times 10^{7}\ Sm^{-1}$ at melting point of 100nm diameter size (~927 ˚C) $2.04 \times 10^{7}\ Sm^{-1}$ at 961^{0}C (Liquid)
$\boldsymbol{\rho}$	Density of silver	$9{,}864\ kg\text{-}m^{-3}$ at melting point of 10nm diameter size (~527 ˚C) $9{,}613\ kg\text{-}m^{-3}$ at melting point of 20nm diameter size (~727 ˚C) $9{,}363\ kg\text{-}m^{-3}$ at melting point of 100nm diameter size (~927 ˚C) $9{,}320\ kg\text{-}m^{-3}$ at 961 ˚C (Liquid)

In Eqs. (20)-(22), the density and electrical conductivity are functions of temperature [48] [49] [50] [51]. Therefore, those are used for calculating a temperature-dependent dielectric permittivity. The co-authors have examined laser spot temperature in small volumes, which indicates very high local temperatures (over 330 ^{0}C) are possible [15]. However, there is no way to directly measure the melting temperature of silver nanoparticles in water at present. Thus, the melting point is calculated using the equation in Fig. 16.

The dielectric permittivity of liquid silver can be derived from those parameters as shown in Table 11 at the temperature of 961^0C [48] [49] [50] [51]. The melting temperature of a silver nanoparticle, however, is a function of particle size due to the increased surface area [29] [30] [31]. Thus, to calculate the dielectric permittivity of solid silver, the values of electrical conductivity and density with reduced melting temperature are used. Based on Eqs. (15)-(24), and the parameters in Table 11, the non-retarded Hamaker constant of water-based silver nanofluid was found by numerically integrating Eq. (16) using the trapezoidal rule in Matlab and is shown in Table 12.

Table 12 Calculated Hamaker Constant Values A132 zJ (zepto Joule, 10^{-21}) at the Melting Temperature of Various-Sized Silver Nanoparticles in Subcooled (25°C) Water.

System	10nm	20nm	100nm
Ag-melt-H_2O	-1.62	-1.05	-0.36

The values of the Hamaker constants in Table 12 indicate the interaction between two interfaces (Ag:melted Ag and melted Ag:water). The negative values indicate repulsion between the interfaces [41]. Table 12 indicates the repulsive force changes in different-sized particles. That is, 10nm-sized particles have stronger repulsive force than 20nm and 100nm-sized nanoparticles. Therefore, if melting would occur around silver

nanoparticles, in this regime, it is possible that a partially or fully melted particle would have a tendency to break apart and form smaller particles [52]. In other words, this would be observable in the form of a size reduction in the particles after heating. Other factors such as unstable particles settling out upon heating or deagglomeration could also lead to particle size reduction. However, if several experiments consistently show a similar particle size reduction after heating, the melting could be a dominant factor. Thus, particle sizes before and after heating experiments were measured to determine if melting is possible in saturated and subcooled aqueous silver nanofluids.

4.1.3 Experimental Approach and Discussion

In order to identify the reduction (if any) of the average particle size after heating, an experimental apparatus was set up with the configuration shown in Fig. 20 [10] [28]. For the nanofluid preparation, the two-step method was employed [10] [15]. At present only 20nm-sized silver nanopowder could be obtained. Thus, 20nm-sized silver nanoparticles, which were purchased from Navecentrix, Inc., were dispersed in deionized (DI) water using a sonicator (model UP200S from Hielscher, GmbH) for the experiments. In addition, 1% by volume sodium dodecyl sulfate (SDS) was added for stabilizing the silver nanoparticles in the DI water [15].

(a)

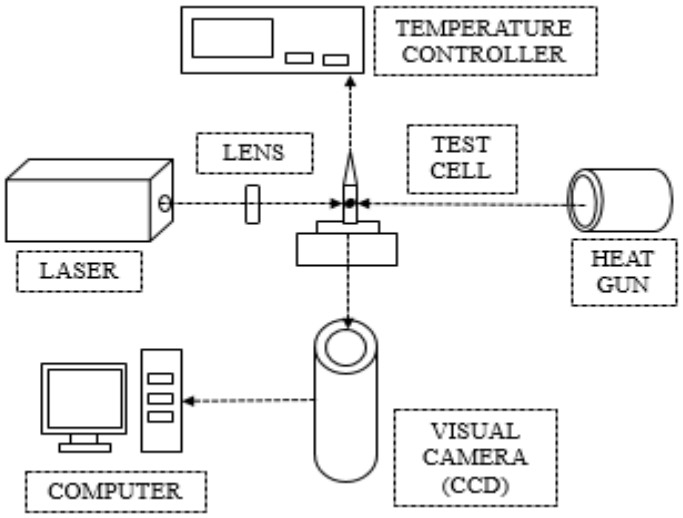

(b)

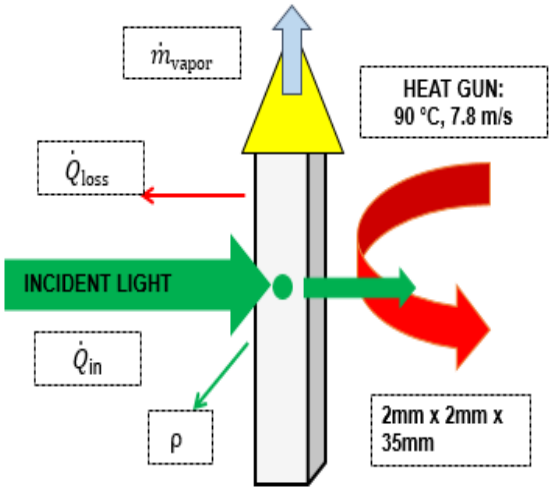

Figure 20. (a) Schematic Diagram of the Set-Up for Boiling Experiment of Silver Nanofluid with Laser (b) Schematic Representation of Test Cell with Thermal and Optical processes

The test cell was a transparent quartz-based square cuvette of size 2mm x 2mm x 35mm as shown in Fig 20 (b). The heat was input by a continuous, 130mW, 532nm laser, and a secondary heat input was provided with an air heat gun to maintain constant surrounding temperatures near the boiling temperature (e.g. 100 ^{0}C) of water. This approach for minimizing heat loss was chosen (over thermal insulation) to maintain optical access to the sample. A 150-mm focal length spherical lens was used to concentrate the input laser light to achieve high irradiance [15]. Bubbles in the test cell were observed with a Retiga charged coupled device (CCD) camera during the experiments. Once the DI water-based silver nanofluid reached the boiling temperature, which took ~1 min using a heat gun, the laser was turned on to illuminate the silver nanofluid for a duration of 20 min. In addition, the laser-based experiment without the air heat gun was also conducted to identify the melting of silver nanoparticles in subcooled fluid temperature. Additional details are provided in [10]. Based on the melting hypothesis with the calculation of the Hamaker constant, which indicates repulsion between the interfaces, a decreased size of particles after the laser heating may imply the melting of silver nanoparticles in water [19]. In order to investigate changes in particle size and morphology, Transmission Electron Microscopy (TEM) and Dynamic Light Scattering (DLS) were employed. Figures. 21 (a) - (c) show the TEM images of unheated/heated silver nanoparticles.

(a)

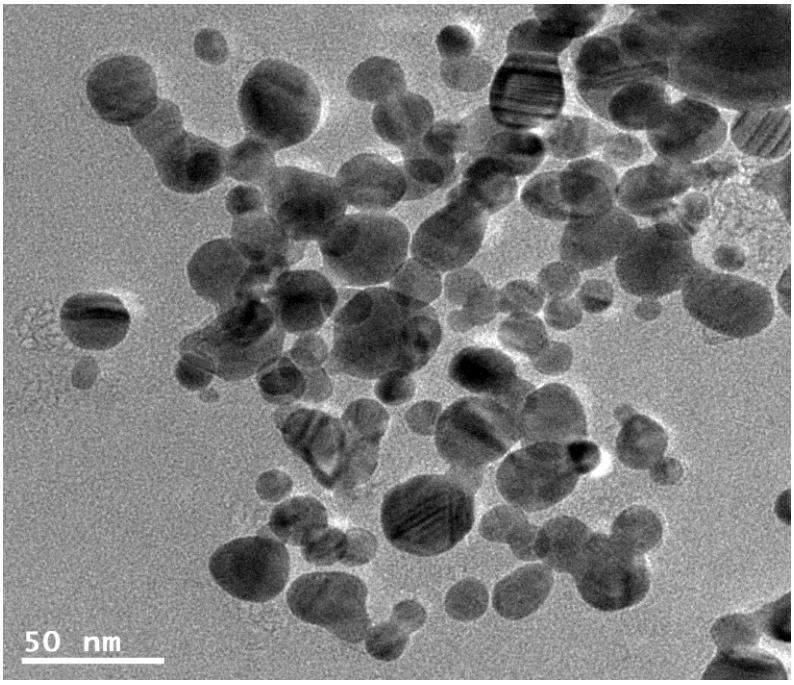

(b)

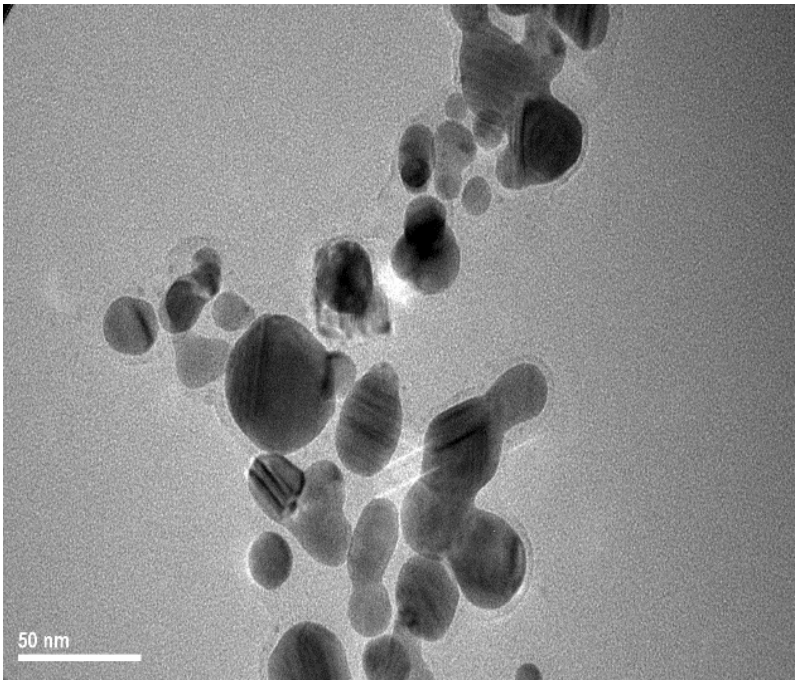

(c)

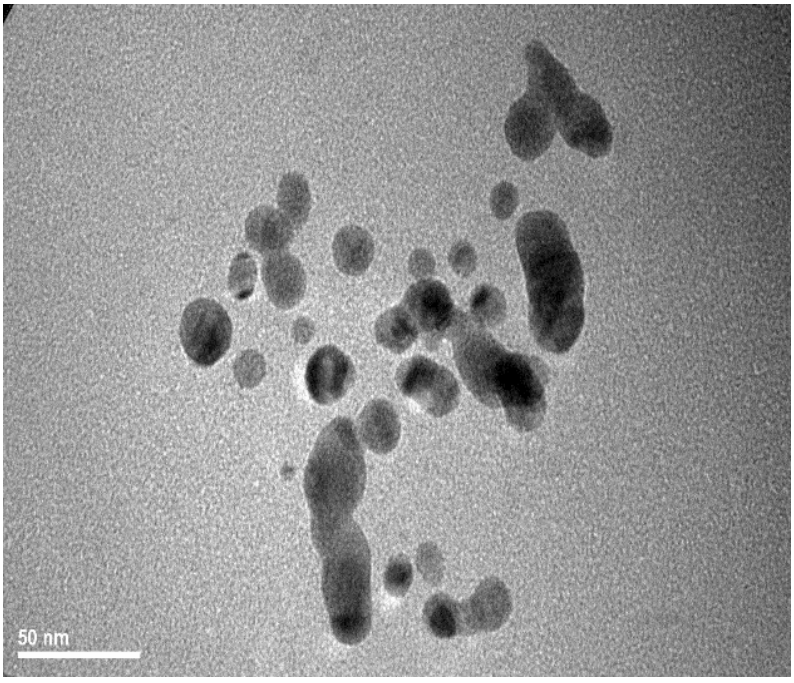

Figure 21. TEM Images of 0.1% by Volume, 20-nm Ag Particles (a) before Heating (b) after Laser Heating in Subcooled Fluid, and (c) after Laser Heating in Saturated Fluid

Particle size distributions (PSDs) from the TEM images in Fig. 22 were measured using Otsu's method and the average size of silver nanoparticles was calculated as shown in Fig. 23 [53].

(a)

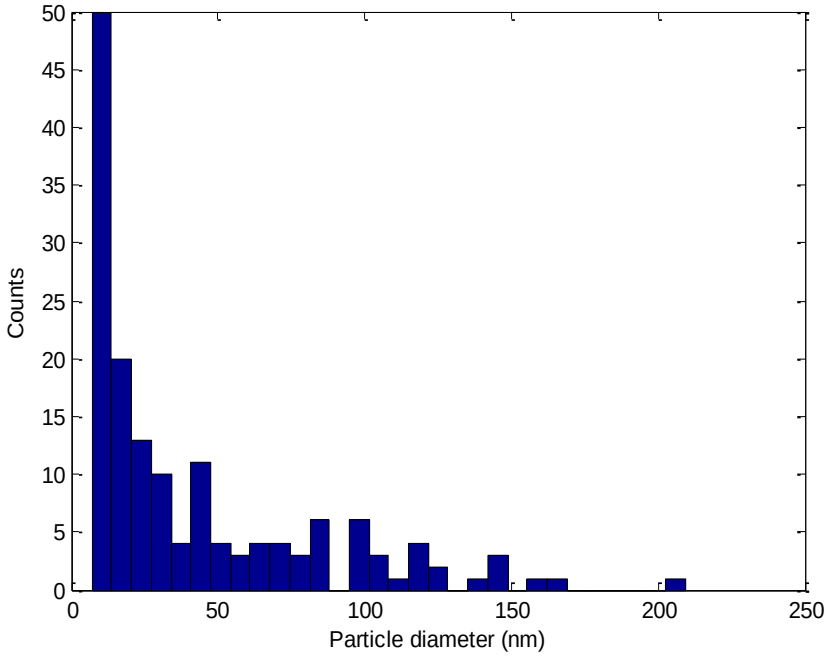
Counts
Particle diameter (nm)
0
5
10
15
20
25
30
35
40
45
50
0
50
100
150
200
250

(b)

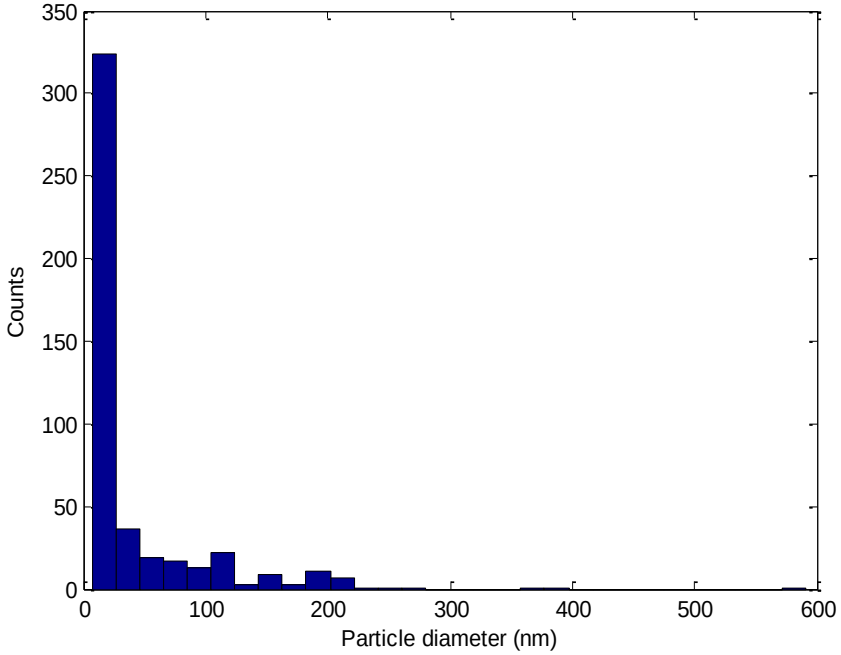
Counts
Particle diameter (nm)
0
50
100
150
200
250
300
350
0
100
200
300
400
500
600

(c)

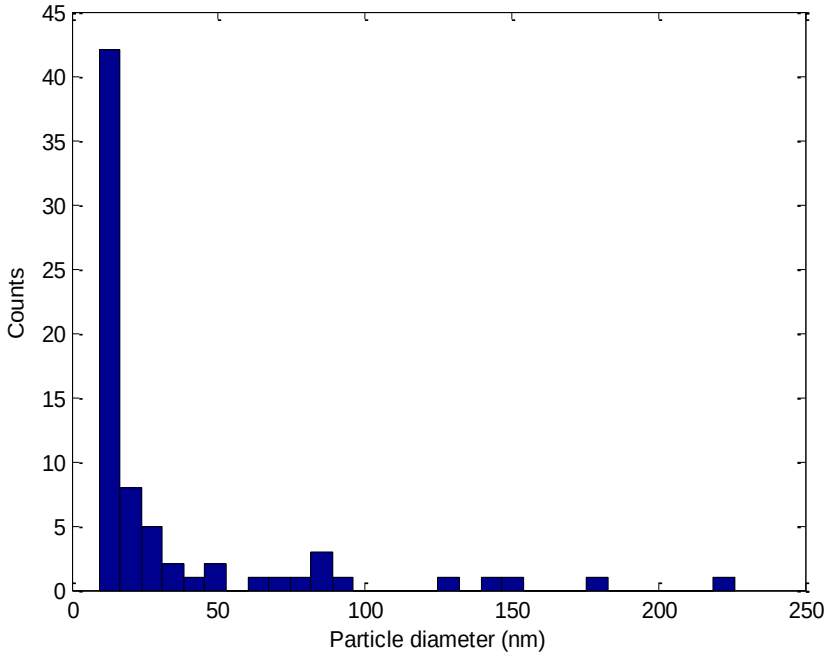

Figure 22. Histograms of Particle Size Distributions Measured from the TEM Images in Figure 5 of (a) Particle Size Distribution before Heating (Mean = 42.9nm) (b) Particle Size Distribution after Laser Heating in Subcooled Fluid (Mean = 41.4nm), and (c) Particle Size Distribution after Laser Heating in Saturated Fluid (Mean =32.5nm)

These results show that the average particle size decreases after laser-based heating, especially for particles suspended in saturated DI water. Thus, surface melting of the particles could be realized in ambient pressure, saturated, and even subcooled water.

(a)

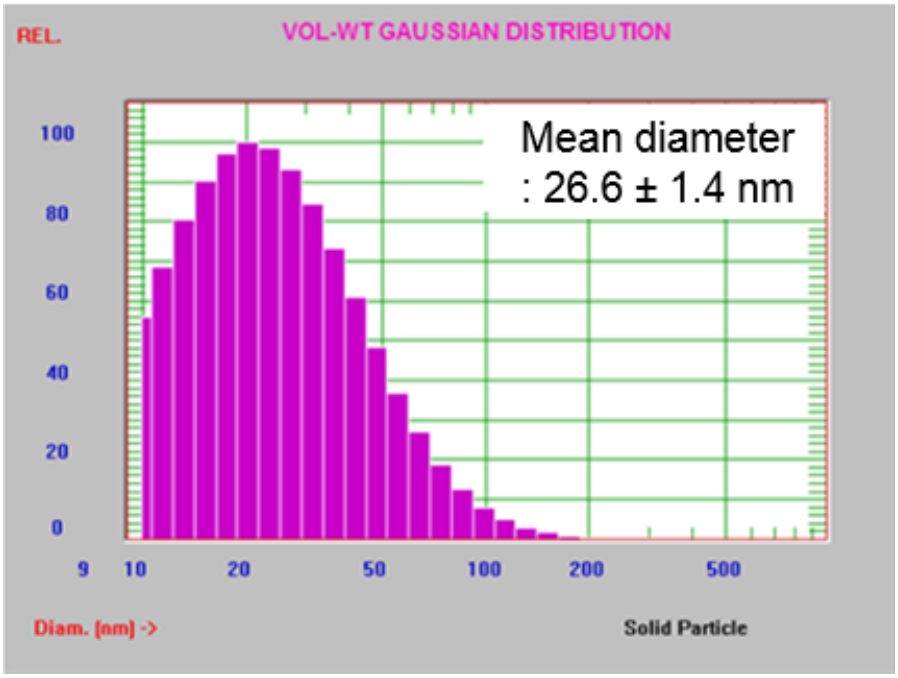
REL.
VOL-WT GAUSSIAN DISTRIBUTION
Mean diameter
: 26.6 ± 1.4 nm
100
80
60
40
20
0
9
10
20
50
100
200
500
Diam. (nm) ->
Solid Particle

(b)

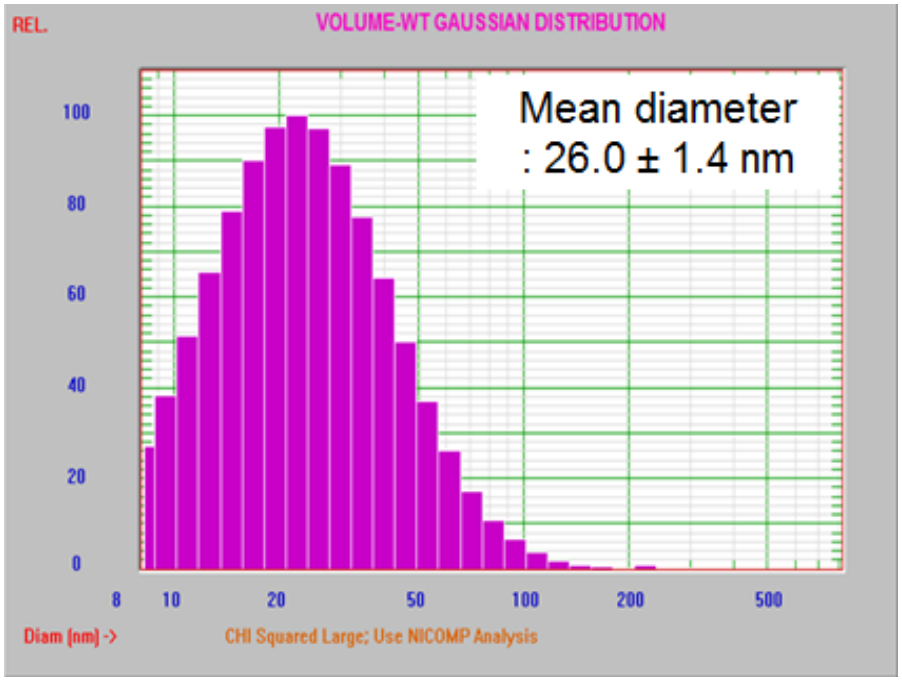
REL.
VOLUME-WT GAUSSIAN DISTRIBUTION
Mean diameter
: 26.0 ± 1.4 nm
100
80
60
40
20
0
8
10
20
50
100
200
500
Diam (nm) ->
CHI Squared Large; Use NICOMP Analysis

(c)

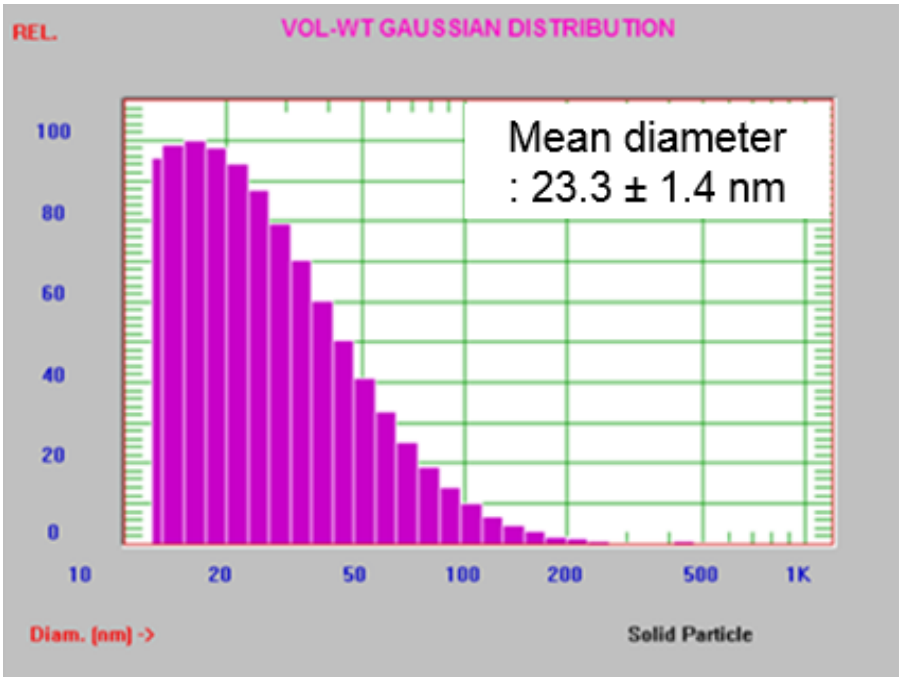

Figure 23. Volume-Weighted Ag Nanoparticles (Initially 20 nm) Size Distribution Measured with Dynamic Light Scattering (DLS, Nicomp 380/ZLS) of 0.1% by Volume Nanofluid (a) before Heating (b) after Laser Heating in Subcooled Fluid, and (c) after Laser Heating in Saturated Fluid

The silver nanofluid samples were also repeatedly measured with DLS, and the results averaged using a volume-weighted distribution method [54]. DLS can maintain the accuracy of measurement to ±3% and was calibrated by its manufacturer. The uncertainty of the experimental data was calculated at the 95% confidence level. Figures 23 (b) and (c) indicate a decrease in particle size in silver nanofluid compared to Fig. 23 (a). The average sizes from the TEM measurements in Fig. 21 are different from those by the DLS

measurements in Fig. 23, perhaps because the number of silver nanoparticles in the measurements is very different. Both sets of results, however, imply that melting of silver nanoparticles could occur during highly concentrated laser heating. As shown in Fig. 22 (b) and Fig. 23 (b) for subcooled fluid, the results indicate only a marginal decrease in the average particle size compared to the unheated samples in Fig. 22 (a) and Fig. 23 (a), respectively, and less than the corresponding results from saturated fluid in Fig. 22 (c) and 23 (c). A possible explanation for this result is that the rate of heat transfer from silver nanoparticles in subcooled water (~70 °C due to the thermal losses) could be much higher than the rate of heat transfer from silver nanoparticles in saturated water (100 °C) [6]. Thus, even though there appears to be melting of silver nanoparticles in subcooled water, the rate of melting could be much lower. Therefore, this effect could contribute to the small observed decrease of average particle size in subcooled fluid compared to that in saturated fluid.

The object of this chapter is to investigate possible melting of silver nanoparticles in water. As such, the Hamaker constant is theoretically analyzed and experiments using silver nanofluid are conducted with TEM and DLS. For this research, surfactant is applied as a stabilizer for the silver nanoparticles in water, however, it could also affect the optical and thermal properties of the nanofluid [10] [19] [43], and therefore could be one of the factors affecting the melting of silver nanoparticles in water. In addition, the morphology of silver nanoparticles could also affect melting, since surface area can be increased by the shape of nanoparticles. Thus, further study is required to investigate the details of the melting of silver nanofluid. Usually, the entropy of the water increases when the hydrogen bonds are broken [19]. From the Hamaker results, the repulsion could occur between

nanoparticles as well as between water molecules and nanoparticles. Therefore, water molecules and nanoparticles could freely move, compared to pure water. That is, the entropy of silver nanofluid increases with surface melting of silver nanoparticles. As a result, this entropy change of silver nanofluid could be a crucial reason for decrease in h_{fg}. Furthermore, silver nanoparticles have a negative effect on human health and the environment since silver nanoparticles appear to be toxic [55], making improved understanding of their melting processes and subsequent size changes an important topic for further research.

4.1.4 Summary

In this dissertation, the Hamaker constant of melted and solid silver nanoparticles in water, which indicates negative values (repulsion) of the interfaces is calculated. That is, if melting is possible in silver nanofluid, the repulsion force may cause the melted part to separate from the remaining solid particle, and therefore a particle size reduction is confirmed. Laser-heated boiling experiments on aqueous silver nanofluids were also conducted and smaller particles after heating were observed based on TEM and DLS. Thus, it is possible that melting of silver nanoparticles in water is occurring. Based on the melting of aqueous silver nanofluids, the interactions between nanoparticles-nanoparticles/nanoparticles-water molecules can be reduced due to the repulsion between silver nanoparticles and water molecules [28]. That is, the repulsion leads to an increase in the entropy of aqueous silver nanofluid. With further experiments, this is relevant to applications where it has been proposed to heat metallic nanoparticles for solar thermal applications and hyperthermia nanomedicine treatments [6] [56] [57] [58].

4.2 Hydrophobic Interactions of Graphite Nanoparticles in Saturated Water

Hydrophobic interactions occur between hydrophobes and water molecules [19]. The main reason for hydrophobic interactions is that water molecules reduces their rotational and translational freedom, which is related to low entropy when water molecules are close to hydrophobes . The low entropy of the water in the interfacial region is caused by the strong directional forces between water molecules [19]. These hydrophobic interactions with low entropy have an impact on h_{fg} [19] [28]. Since graphite is a hydrophobic material, the theoretical investigation of the interactions between graphite nanoparticles and water molecules in aqueous graphite nanofluid could be helpful to determine the hydrophobic interactions of aqueous graphite nanofluids. In general, when hydrophobes (graphite nanoparticles) are placed in water, hydrogen bonds between water molecules are broken to make room for them without a chemical reaction [19]. Then, the water molecules' structure is distorted by the presence of the graphite nanoparticles. As a result, this makes a new hydrogen bond, which is an ice-like cage (clahrate) structure around agglomerated hydrophobes, as shown in Fig. 24 [19] [59] [60] [61]. This structure makes the system more stable, thus the entropy of the fluid could be decreased [19] [62].

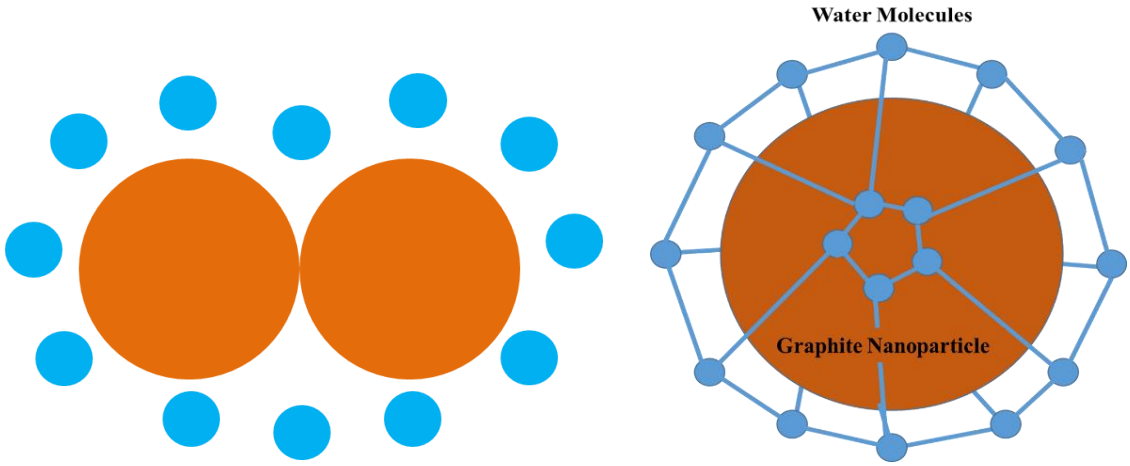

Figure 24. Clathrate Structure by Presence of the Graphite Nanoparticles in Pure Water

That is, based on Eq. (14), h_{fg} can be increased because the entropy of the liquid is decreased due to the hydrophobic interactions between the graphite nanoparticles and water molecules. The decreased liquid entropy leads to an increase of the total entropy, i.e., S_{fg} ($=S_g-S_f$) if the entropy of the vapor is the same as that of pure water. The hydrophobic interactions are relatively stronger than van der Waals interactions or hydrogen bonds [19]. Also, adding hydrophobes in water makes both hydrophobic bonds and existing hydrogen bonds stronger [63] [64]. Therefore, it could be a cause of the high (~30%) h_{fg} increase at 0.1 % by volume aqueous graphite nanofluid, compared to the value of pure water as suggested in Chapter 2.

In addition, the strength of hydrophobic interactions depends on temperature, the number of carbons on the hydrophones, and the shape of the hydrophobes [19] [59]. The strength of the hydrophobic interactions greatly increases as temperature increases due to

the enhancement of the reactions between hydrophobes. Also, the large number of carbon atoms could make the hydrophobic interactions even stronger. Lastly, the shape has something to do with the contact area between the hydrophobes and water molecules.

From the experiments, the laser spot temperature for laser-heated sample was relatively high, ~300 °C [15]. Therefore, the temperature of the graphite nanoparticles could increase up to that point since heat transfer from the nanoparticles to the liquid could be limited due to the vapor layer around nanoparticles [16] [17]. Thus, a structural change of the water molecules (stable hydrogen bonds) could actively occur, and it could make not only the hydrogen bonds stronger, but also the entropy change of aqueous graphite nanofluid reduced, which leads to an increase in the total entropy (S_{fg}). As a result, h_{fg} in aqueous nanofluid could be significantly increased even with a small amount (0.1% volume fraction) of graphite nanoparticles in water. Contrary to the repulsion between nanoparticles in silver nanofluid, agglomeration between nanoparticles in graphite nanofluid is likely to occur. Due to this reason, the structure of hydrogen bond changes in graphite nanofluid leads to the reduction of liquid entropy. In sum, h_{fg} in silver nanofluid and graphite nanofluid decreased and increased, respectively, due to the different entropy changes in the liquid nanoparticle suspensions.

CHAPTER 5. SOLAR THERMAL APPLICATION

In this section, applying the modified h_{fg} results of graphite and silver nanofluids in a solar thermal system is proposed to investigate the performance of the system. The h_{fg} results in Chapter 2 indicate that h_{fg} can be increased or decreased by adding graphite or silver nanoparticles in water. The decreased h_{fg} in aqueous silver nanofluids could be beneficial for real-world solar thermal collectors because more vapor from silver nanofluid can be obtained, compared to that of pure water. Therefore, a silver nanofluid-based solar thermal collector could lead to improve system thermal efficiency. This section discusses the applicability of efficient aqueous silver nanofluid-based solar thermal collectors with the increased h_{fg} . In addition, the increased h_{fg} in graphite nanofluid could be used for enhancing thermal storage capability because the graphite nanofluid can be used to store more thermal energy than pure water. Therefore, solar thermal storage based on graphite nanofluid is also discussed in this section,

5.1 Vapor Power Systems - Rankine Cycle

Since only water-based nanofluids are considered in this dissertation, steam Rankine thermal cycles are appropriate to investigate the applicability of silver nanofluid as a working fluid in solar thermal system. The Rankine cycle is the fundamental operating cycle for plants that include fluid evaporation and condensation processes [33], as shown in Fig. 25. Since the Rankine cycle consists of internally reversible processes, the working fluid is considered to pass through the internally reversible proceses, i.e. insentropic

expansion through the turbine, insentropic compression in the pump, and heat transfer at boiler and condenser at constant pressure.

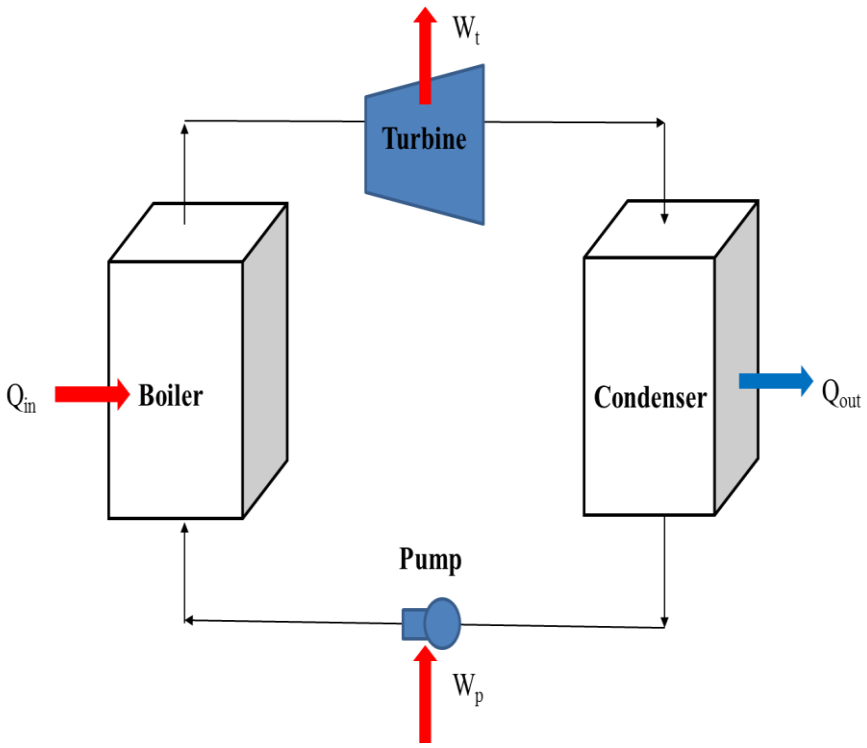

Figure 25. Typical Rankine Cycle

5.2 Nanofluid-Based Solar Thermal Collector

Most electrical generating vapor power plants employ water as the working fluid because it is stable and easy to use. [33] Therefore, aqueous nanofluids with small volume fractions could be employed to increase the overall efficiency of the plants. As shown in Fig. 26, the overall Rankine cycle-based plants consist of four major subsystems, i.e., boiler,

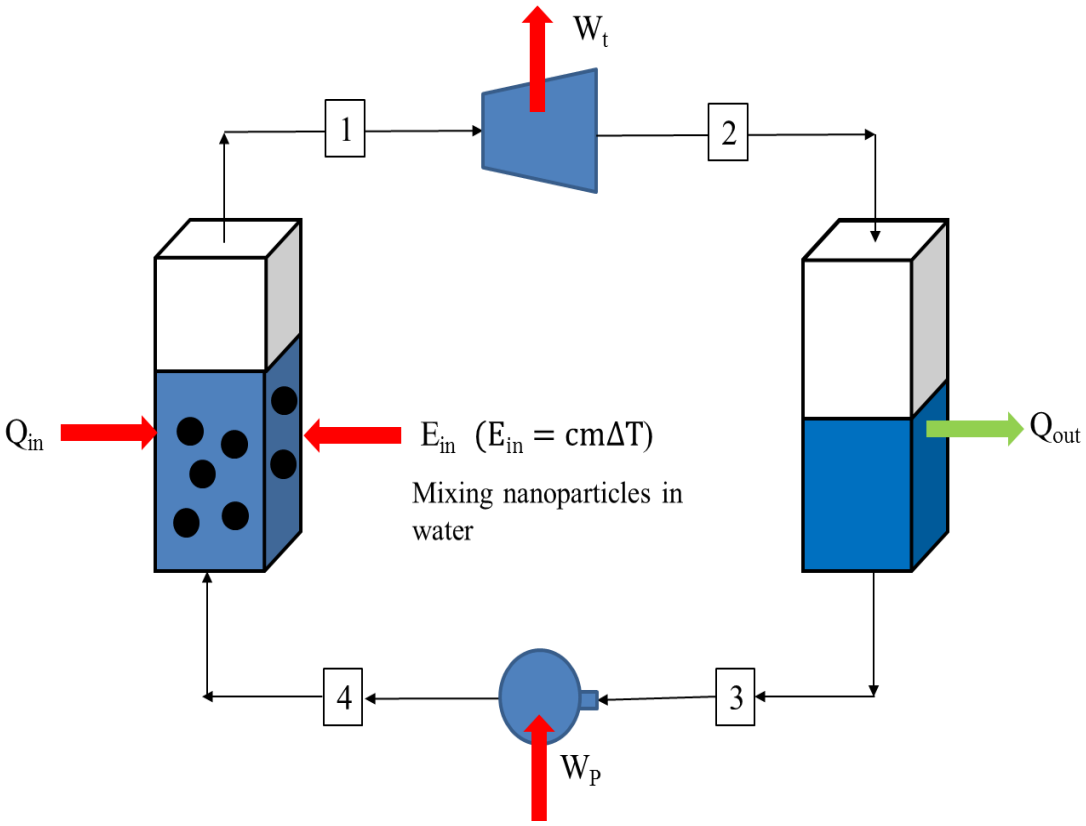

Figure 26. Components of a Nanofluid-Based Solar Thermal System

turbine, condenser, and pump [33]. The volumetric aqueous silver nanofluid-based solar thermal collector acts as both a collector and a boiler. It is used for generating vapor by capturing sunlight, and then the vapor exits to the turbine to generate electricity. Then, the vapor passes through the condenser, where it condenses to saturated liquid water (pure, with no nanoparticles). Finally, the saturated pure liquid water goes back to the collector, is mixed with the remaining highly concentrated nanofluid, and repeats the cycle [33].

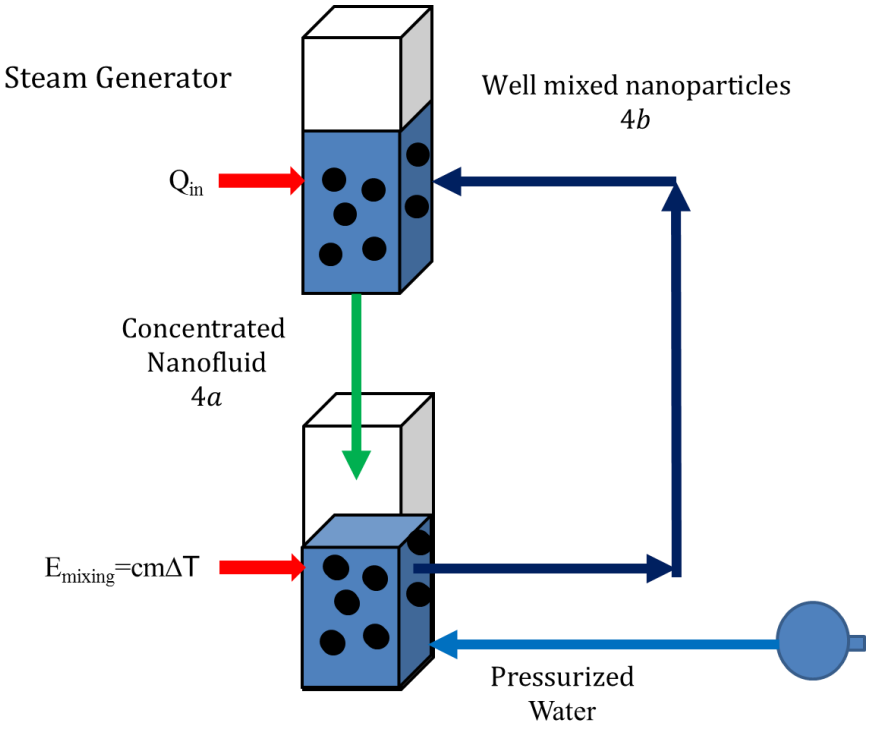

Figure 27. Preparation of Silver Nanofluids in a Cycle

In Fig. 26, state point 1 is pure saturated water vapor, state point 2 is a two-phase mix of pure liquid water and vapor, state point 3 is pure saturated liquid water, and state point 4 is pure compressed liquid water. The values of heat transfer and work can be obtained by applying the first law of thermodynamics to each process. Figure 27 indicates how to prepare silver nanofluid in a cycle. Nanoparticles are assumed to remain in the collector, where they are mixed with pressurized water from the pump. Then, the well-mixed silver nanofluid returns to the collector to generate vapor. Compared to the heat input, the mixing energy is relatively small. Therefore, it is ignored in this section. In this Rankine cycle, the work of the turbine (W_t) assuming isentropic expansion can be calculated by:

$$\dot{W}_t = \dot{m}\,(h_1 - h_2) \tag{25}$$

where $\dot{m}$ is the mass flow rate, and h the enthalpy. In the condenser, the rate of heat transfer ($\dot{Q}_{out}$) from the vapor to cooling water can be evaluated:

$$\dot{Q}_{out} = \dot{m}\,(h_2 - h_3) \tag{26}$$

At the pump, the liquid is pumped from the condenser to the high pressure boiler and the work of the pump is given by:

$$\dot{W}_P = \dot{m}\,(h_4 - h_3) \tag{27}$$

The working fluid completes the cycle from the compressed liquid exiting the pump to the volumetric solar thermal collector. The rate of heat transfer to the volumetric solar thermal collector is:

$$\dot{Q}_{in} = \dot{m}\,(h_1 - h_4) \tag{28}$$

The thermal efficiency of the cycle (η) is defined as:

$$\eta = 1 - \frac{\dot{Q}_{out}/\dot{m}}{\dot{Q}_{in}/\dot{m}} = 1 - \frac{(h_2 - h_3)}{(h_1 - h_4)} \tag{29}$$

In Fig. 27, nanoparticles are assumed to stay in the solar thermal collector during a cycle. Therefore, nanoparticles in the water could only affect state 1 (h_1), assuming that the pressure and corresponding saturation temperature at state 1 changes as a result of increased or decreased mass flow rate. When h_{fg} decreases using silver nanofluid, relatively more vapor can be generated in the collector. This could lead to increased pressure of state 1, relative to the pure water case, and the increased pressure leads to an increase in temperature. As a result, the enthalpy of the saturated vapor can be increased. Based on Eq. (29), theoretically, when h_1 increases, the thermal efficiency also increases. That is, the thermal efficiency could theoretically increase based on silver nanofluid relative to that for pure water, assuming an increase in saturation pressure leaving the collector. Based on Eq. (30), when the turbine work varies in terms of h_1, the heat transfer input also varies with h_1.

$$\dot{W}_{cycle} = \dot{W}_t - \dot{W}_P = \dot{Q}_{in} - \dot{Q}_{out} \tag{30}$$

Therefore, this cycle is not violating the first law of thermodynamics because energy and mass are conserved during a cycle.

5.3 Nanofluid-Based Solar Thermal Storage

In residential buildings, water-based heat storage systems connected to the solar thermal collector are used as shown in Fig. 28 [33].

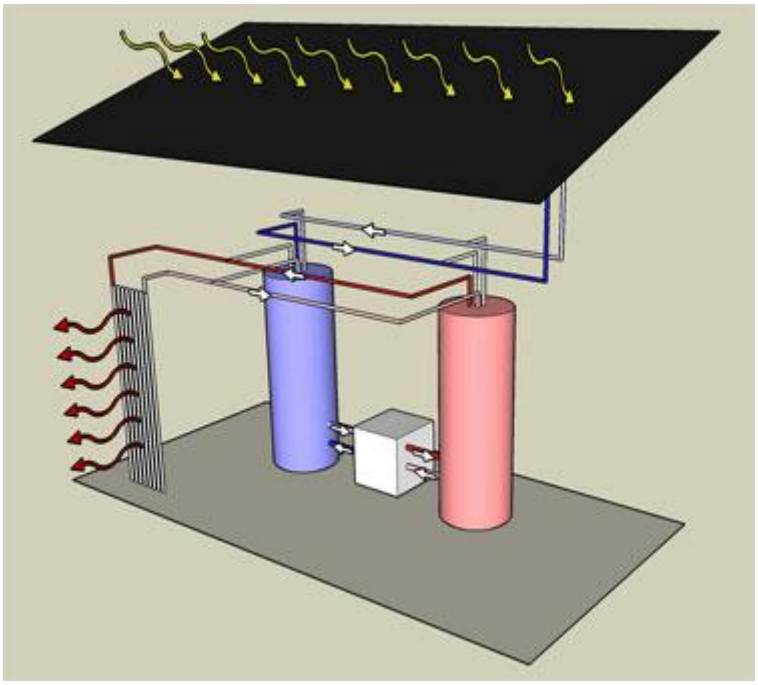

Figure 28. Schematic of Solar Thermal Storage in a House (http://solar.colorado.edu/design/hvac.html)

In order to store more energy, a phase change material (PCM) such as water is employed because latent heat is much higher than the specific heat. Therefore, water can release considerable energy when it is needed. Since h_{fg} of aqueous graphite nanofluid can be significantly increased by sunlight compared to that of pure water, relatively more energy can be stored in a storage tank. From this result, the efficiency of the system can be increased, or the same amount of energy can be stored more compactly. In sum, the

applicability of aqueous nanofluids instead of pure water is investigated. These studies are mostly based on a qualitative explanation. Therefore, in order to validate the results, nanofluids-based experiments with the actual system should be conducted as a future work.

CHAPTER 6. CONCLUSIONS AND SUGGESTIONS FOR FUTURE WORK

In the last few decades, many researchers have focused on nanotechnology as a means of enhancing the performance of various applications in electronics, photonics, and solar energy. Therefore, nanofluids, suspensions of submicron-sized (<100nm) nanoparticles in fluids, have been extensively investigated because of their potentially enhanced thermal properties, i.e., thermal conductivity, convective heat transfer, and latent heat. Recently, vapor generation around nanoparticles in water from volumetric energy sources (e.g. concentrated sunlight and laser light) has been presented, and it opens the possibility to manipulate h_{fg} in nanofluids. Therefore, we conducted experiments to verify that h_{fg} in aqueous nanofluids can be varied, depending on the type of nanoparticle. These results indicated that h_{fg} of water can be increased or decreased by low-volume-fraction aqueous graphite and silver nanofluids, respectively. It means that the variation of h_{fg} in aqueous nanofluids can potentially be applied to direct absorption solar thermal collectors and latent heat-based thermal storage, since the results can enhance not only the light-to-thermal energy conversion, but also stored energy density. Also, further experiments with changing surface area based on volume fraction (0.005% to 2%) and various nanoparticle sizes to investigate the mechanisms for h_{fg} modification in aqueous graphite and silver nanofluids are reported. To support the experimental results, a theoretical approach based on measured thermophysical properties is presented. In addition, nanoscale studies to explain the entropy changes of the liquids are presented. In this dissertation, hydrophobic interactions in graphite nanofluid are introduced to explain the increase of h_{fg} in aqueous

graphite nanofluid. However, advanced simulation methods, i.e., MD simulations, are not discussed in this dissertion. A quantitative estimate of the hydrophobic interactions between graphite nanoparticles and water molecules would likely require an MD simulation [65]. That is, based on an MD simulation, the entropy change in the fluid and thermophysical properties, i.e., density and surface tension, could be obtained theoretically. Therefore, this work could be done to improve understanding of the increase of h_{fg} in aqueous graphite nanofluid as future work [66] Also, in Chapter 5, the applicability of aqueous nanofluids to volmetric solar thermal collectors and solar thermal storage, exploiting the changes in h_{fg}, is investigated.

Therefore, in the future, it is required to design and conduct experiments in a real Rankine cycle to investigate the efficiency of the suggested silver nanofluid-based solar thermal collector, as well as graphite nanofluid-based solar thermal storage.

REFERENCES

[1] M. Mehrali, E. Sadeghinezhad, S. T. Latibari, S. N. Kazi, M. Mehrali, M. N. Zubir and H. S. Metselaar, "Investigation of Thermal Conductivity and Rheological Properties of Nanofluids Containing Graphene Nanolatelets," *Nanoscale Research Letters,* vol. 9, no. 15, 2014.

[2] Z. Haddad, C. Abid, H. F. Oztop and A. Mataoui, "A Review on How the Researchers Prepare their Nanofluids," *Int. J. Therm. Sci,* vol. 76, pp. 168-189, 2014.

[3] R. A. Taylor and P. E. Phelan, "Pool boiling of nanofluids: Comprehensive review of existing data and limited new data," *Int. J of Heat and Mass Transfer,* vol. 52, pp. 5339-5347, 2009.

[4] S. Thomas and C. B. Sobhan, "A review of experimental investigations on thermal phenomena in nanofluids," *Nanoscale Res. Lett.,* vol. 6, p. 377, 2011.

[5] R. Prasher, P. Bhattacharya and P. E. Phelan, "Thermal Conductivity of Nanoscale Colloidal Solutions (Nanofluids)," *Phys. Rev. Lett.,* vol. 94, no. 025901, 2005.

[6] S. Krishnamurthy, P. Bhattacharya and P. E. Phelan, "Enhanced Mass Transport in Nanofluids," *Nano Lett.,* vol. 6, pp. 419-423, 2005.

[7] M. M. Ameen, K. Prabhul, G. Sivakumar, P. P. Abraham, U. B. Jayadeep and C. B. Sobhan, "Molecular Dynamics Modeling of Latent Heat Enhancement in Nanofluids," *Int. J. Thermophys,* vol. 31, pp. 1131-1144, 2010.

[8] R. Taylor , S. Coulombe, T. Otanicar, P. Phelan, A. Gunawan, W. Lv, G. Rosengarten, R. Prasher and H. J. Tyagi, "Small Particles, Big Impacts: A Review of the Diverse Applications of Nanofluids," *J. Appl. Phys.,* vol. 113, no. 011301, 2013.

[9] P. Phelan, T. Otanicar, R. Taylor and H. Tyagi, "Trends and Opportunities in Direct-Absorption Solar Thermal Collectors," *J. Therm. Sci. Eng. Appl.,* vol. 5, no. 021003, 2013.

[10] S. Lee, P. E. Phelan, L. Dai, R. Prasher, A. Gunawan and R. A. Taylor, "Experimental Investigation of the Latent Heat of Vaporization in Aqueous Nanofluids," *Appl. Phys. Lett.,* vol. 104, pp. 1-4, 2014.

[11] R. Chen, T. X. Phuoc and D. Martello, "Effects of Nanoparticles on Nanofluid Droplet Evaporation," *Int. J. of Heat and Mass Trans.,* vol. 53, pp. 3677-3682, 2010.

[12] B. J. Zhu, W. L. Zhao, J. K. Li, Y. X. Guan and D. D. Li, "Thermophysoical Properties of Al2O3-Water Nanofluids," *Mat. Sci. Forum,* vol. 688, pp. 266-271, 2011.

[13] S. Harikrishnan and S. Kalaiselvam, "Experimental Investigation of Solidification and Melting Characteristics of Nanofluid as PCM for Solar Water Heating Systems," *Int. J. of Emer. Tech. and Adv. Engi.,* vol. 3, pp. 628-635, 2013.

[14] M. Mehregan and M. Moghiman, "Propose a Correlation to Approximate Nanofluids' Enthalpy of Vaporization - A Numerical Study," *Int. J. of Mat. Mech. and Manu.,* vol. 2, pp. 73-76, 2014.

[15] R. A. Taylor, P. E. Phelan, R. J. Adrian, A. Gunawan and T. P. Otanicar, "Characterization of Light-Induced, Volumetric Steam Generation in Nanofluids," *Int. J. Therm. Sci.,* vol. 56, pp. 1-11, 2012.

[16] R. A. Taylor, P. E. Phelan, T. Otanicar, R. J. Adrian and R. S. Prasher, "Vapor generation in a nanoparticle liquid suspension using a focused, continuous laser," *Appl. Phys. Lett.,* vol. 98, p. 161907, 2009.

[17] O. Neumann, A. S. Urban, J. Day, S. Lal, P. Nordlander and N. Halas, "Solar Vapor Generation Enabled by Nanoparticles," *ACS Nano,* vol. 7, pp. 42-49, 2013.

[18] J. Barber, D. Brutin and L. Tadrist, "A Review on Boiling Heat Transfer Enhancement with Nanofluids," *Nanoscale Research Letters,* vol. 6, pp. 1-13, 2011.

[19] J. N. Israelachvili, Intermolecular and Surface Forces 3rd ed, Academic Press, 2011.

[20] L. Soochan, R. A. Taylor, L. Dai, R. Prasher and P. E. Phelan, "The Effective Latent Heat of Aqueous Nanofluids," *Materials Research Express,* p. 065004, 2015.

[21] V. P. Carey, Liquid-Vapor Phase-Change Phenomena, New York: Taylor & Francis, 2008.

[22] R. A. Taylor, P. E. Phelan, P. T. Otanicar, R. Adrian and R. Prasher, "Nanofluid Optical Property Characterization: Towards Efficient Direct Absorption Solar Collector," *Nanoscale Research Letters,* vol. 6, pp. 1-11, 2011.

[23] T. A. Cengel and A. J. Ghajar, Heat and Mass Transfer, New York, USA: McGraw-Hill, 2011.

[24] S. Figliola and D. E. Beasley, Theory and Design for Mechanical.

[25] J. Garai, "Physical model for vaporization," *Fluid Phase Equilibria,* vol. 283, pp. 89-92, 2009.

[26] V. P. Carey, Liquid Vapor Phase Change Phenomena: An Introduction to the Thermophysics of Vaporization and Condensation Processes in Heat Transfer Equipment, CRC Press, 2007.

[27] C. Gerardi, D. Cory, J. Buongiorno, L. Hu and T. McKrell, "Nuclear Magnetic Resonance-Based Study of Ordered Layering on the Surface of Alumina Nanoparticles in Water," *Appl. Phys. Lett.,* vol. 95, no. 253104, 2009.

[28] S. Lee, P. E. Phelan, R. A. Taylor, R. Prasher and L. Dai, "Low-Temperature Melting of Silver Nanoparticles in Subcooled and Saturated Water," in *ASME IMECE-36963*, Montreal, Canada, 2014.

[29] T. Yonezawa, S. Arai, H. Takeuchi, T. Kamino and K. Kuroda, "Preparation of naked silver nanoparticles in a TEM column and direct in situ observation of their structural changes at high temperature," *Chem. Phys. Lett.,* vol. 537, pp. 65-68, 2012.

[30] Y. Qin, M. Hu, H. Li, Z. Zhang and Q. Zou, "Preparation and Field Emission Properties of Carbon Nanotubes Cold Cathode using Melting Ag Nano-Particles as Binder," *Applied Suface Science,* vol. 253, pp. 4021-4024, 2007.

[31] J. Sun and S. L. Simon, "The Melting Behavior of Aluminum Nanoparticles," *Thermochimica Acta.,* vol. 463, pp. 32-40, 2007.

[32] C. L. Chen, J. Lee, K. Arakawa and H. Mori, "In Situ Observations of Crystalline-To-Liquid and Crystalline-To-Gas Transitions of Substrate-Supported Ag Nanoparticles," *Appl. Phys. Lett.,* vol. 96, pp. 2531041-2531043, 2010.

[33] Y. Cengel and M. Boles, Thermodynamics: An Engineering Approach, New york, USA: McGraw-Hill, 2010.

[34] D. S. Viswanath and N. R. Kuloor, "On Latent Heat of Vaporization, Surface Tension, and Temperature," *J of Chem. and Engi. Data,* vol. 11, pp. 69-72, 1966.

[35] K. S. Birdi, Surface and Colloid Chemistry, Boca Raton, FL, USA: CRC Press, 2009.

[36] Z. Said, M. Sajid H, A. Kamyar and R. Saidur, "Experimental Investigation on the Stability and Density of TiO2, Al2O3, SiO2 and TiSiO4," *Earth and Environmental Science,* vol. 16, no. 012002, 2013.

[37] K. K. Nanda, "Size-dependent Melting of Nanoparticles: Hundred Years of Thermodynamic Model," *J. Phys.*, vol. 72, pp. 617-628, 2009.

[38] J. Drelich, "Nanoparticles in a Liquid: New State of Liquid?," *J Nanomater. Mol. Nanotechnol.,* vol. 2, pp. 1-2, 2013.

[39] A. O. Pinchuk, "Size-Dependent Hamaker Constant for Silver Nanoparticles," *J. Phys. Chem. C,* vol. 116, pp. 20099-20102, 2013.

[40] R. H. French, R. M. Cannon, L. K. DeNoyer and Y.-M. Chiang, "Full Spectral Calculation of Non-Retarded Hamaker Constants for Ceramic Systems from Interband Transition Strengths," *Solid State Ionics,* vol. 75, pp. 13-33, 1995.

[41] X. J. Chen, A. C. Levi and E. Tosatti, "Hamaker Constant Calculations and Surface Melting of Metals," *Surface Science,* vol. 251, pp. 641-644, 1991.

[42] Z. Fang, Y.-R. Neumann, O. Polman, A. Garcia de Abajo, P. Nordlander and N. J. Halas, "Evolution of Light-induced Vapor Generation at a Liquid-immersed Metallic Nanoparticle," *Nano Lett.,* vol. 13, pp. 1736-1742, 2013.

[43] C. F. Boheren and D. R. Huffman, Absorption and Scattering of Light by Small Particles, New York: Wiley, 1998.

[44] P. T. Otanicar, P. E. Phelan, S. R. Prasher, G. Rosengarten and R. A. Taylor, "Nanofluid-based Direct Absorption Solar Collector," *J Renewable Sustainable Energy,* vol. 2, pp. 03310201-03310213, 2010.

[45] G. M. Hale and M. R. Query, "Optical Constants of Water in the 200nm to 200um Wavelength Resion," *Appl. Opt.,* vol. 12, pp. 555-558, 1973.

[46] E. D. Palik, Handbook of Optical Constants of Solids, Orlando, FL, USA: Academic Press, 1985.

[47] P. Schiebener, J. Straub and J. M. Levelt Sengers, "Refractive Index of Water and Steam as Funtion of Wavelength, Temperature, and Density," *J Phys. Chem. Ref. Data,* vol. 19, pp. 677-717, 1990.

[48] M. Schmid, S. Zehnder, P. Schwaller, B. Neuenschwander, J. Zurcher and U. Hunziker, "Measuring the Complex Refactive Index of Metals in the Solid and Liquid State and its Influence on the Laser Machining," in *Proc. of SPIE,* 2013.

[49] M. Bruckner, J. H. Schafer, C. Schiffer and J. Uhlenbusch, "Measurement of the Optical Constants of Solid and Molten Gold and Tin at v=10.6 um," *J Appl. Phys.,* vol. 70, pp. 1642-1647, 1991.

[50] M. Bruckner, J. H. Schafer and J. Uhlenbusch, "Ellipsometric Measurement of the Optical Contants of Solid and Molten Aluminum and Copper at v-10.6 um," *J Appl. Phys.,* vol. 66, pp. 1326-1332, 1989.

[51] R. A. Matula, "Electrical Resistivity of Copper, Gold, Palladium, and Silver," *J Phys. Chem. Ref. Data,* vol. 4, pp. 1257-1297, 1979.

[52] E. A. Olson, N. Y. Efremov, M. Zhang, Z. Zhang and L. H. Allen, "Size-dependent Melting of Bi Nanoparticles," *J Appl. Phys.*, vol. 97, no. 034304, 2005.

[53] L. C. Gontard, D. Ozkaya and R. E. Dunin-Borkowsk, "A Simple Algorithm for Measuring Particle Size Distributions on an Uneven Background from TEM images," *Ultramicroscopy,* vol. 111, pp. 101-106, 2011.

[54] W. Y. Lai, S. Vinod, P. E. Phelan and R. Prasher, "Convective Heat Transfer for Water-Based Alumina Nanofluids in a Single 1.02-mm Tube," *J Heat Transfer,* vol. 131, pp. 112401-112409, 2009.

[55] P. S. Bharadwaj, "Silver or Silver Nanoparticle A Safety or A Risk," *J Environ. Res. Develp.*, vol. 7, pp. 452-456, 2012.

[56] M. Elimelech, J. Gregory, X. Jia and R. Williams, Particle Deposition and Aggregation: Measurement, Modeling and Simulation, Butterworth-Heinemann, UK, 1998.

[57] L. Novotny and B. Hecht, Principle of Nano Optics, New York, USA: Cambridge University Press, 2006.

[58] C. Tang, Y.-M. Sung and L. Junho, "Nonlinear Size-dependent Melting of the Silica-encapsulated Silver Nanoparticles," *J Appl. Phys. Lett.,* vol. 100, pp. 2019031-2019033, 2012.

[59] E. E. Meyer, K. J. Rosenberg and J. Israelachvili, "Recent Progress in Understanding Hydrophobic Interactions," *PNAS,* pp. 15739-15746, 2006.

[60] Y. I. Tarasevich, "State and Structure of Water in Vicinity of Hydrophobic Surfaces," *Colloid Journal,* pp. 248-258, 2011.

[61] E. G. Strekalova, M. G. Mazza, H. E. Stanley and G. Franzese, "Hydrophobic Nanoconfinement Suppresses Fluctuations in Supercooled Water," *J of Phys. Condens. Matter* , p. 064111, 2012.

[62] L. F. Scatena, M. G. Brown and G. L. Richmond, "Water at Hydrophobic Surfaces: Weak Hydrogen Bonding and Strong Orientation Effects," *Science,* pp. 908-912, 2001.

[63] M. P. Williamson and D. H. Williams, "Hydrophobic Interactions Affect Hydrogen bond strengths in Complexes between Peptides and Vancomycin or Ristocetin," *J Biochem.*, pp. 345-348, 1984.

[64] L. Li, D. Bedrov and G. D. Smith, "Water-Induced Interactions between Carbon Nanoparticles," *J Phys. Chem. B,* pp. 10509-10513, 2006.

[65] T. M. Raschke, J. Tsai and M. Levitt, "Quantification of the Hydrophobic Interaction by Simulations of the Aggregation of Small Hydrophobic Solutes in Water," *PNAS,* pp. 5965-5969, 2001.

[66] D. A. Doshi, E. B. Watkins, J. N. Israelachvili and J. Majewski, "Reduced Water Density at Hydrophobic Surfaces: Effect of Dissolved Gases," *PNAS,* pp. 9458-9462, 2005.

APPENDIX A

REFLECTANCE AND THERMAL LOSS CALCULATIONS

The optical loss (reflection) from the front of the cuvette with nanofluids is shown in Fig. A1.

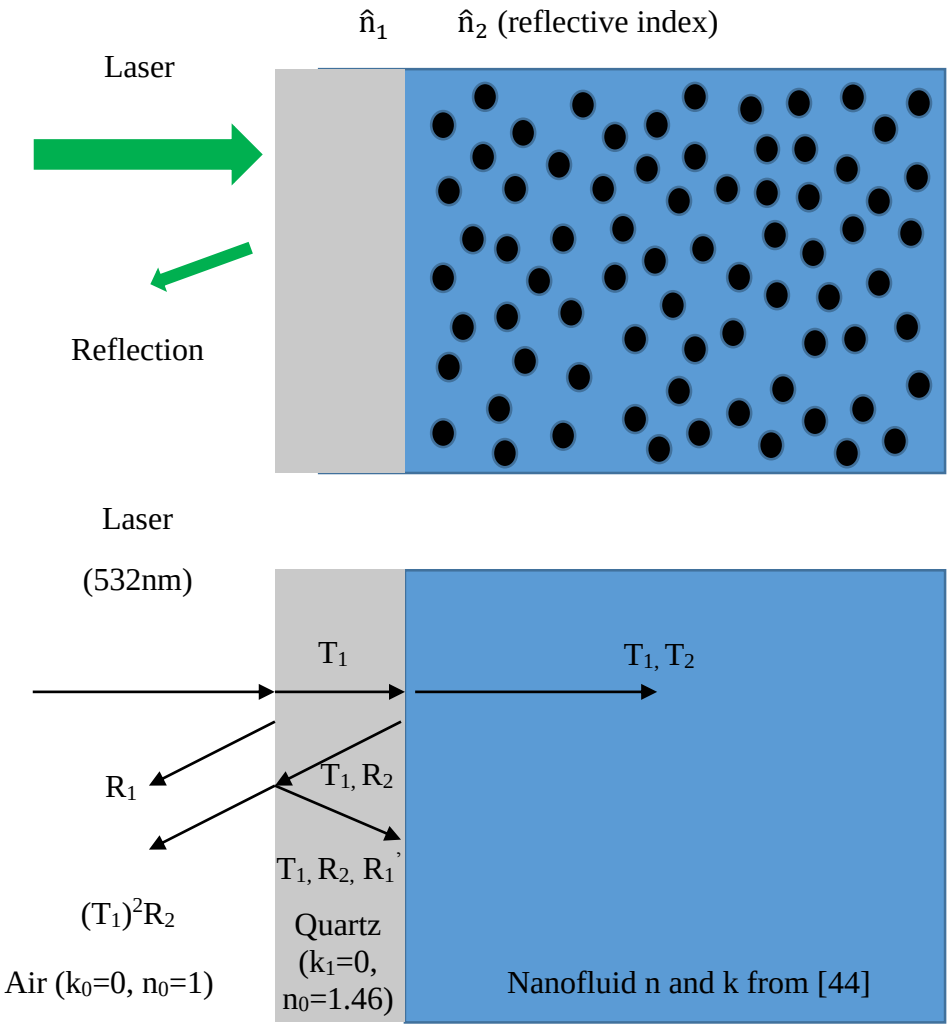

Figure A1. Refelction Calculation of Nanofluid in Quartz-Based Test Cuvette

Due to $R_1 = R_1'$(internal reflection), R can be derived as:

$$R = R_1 + \frac{T_1^2 R_2}{1 - R_2 R_1}$$

where

$$R_i = \frac{(n_j - n_i)^2 + (k_j - k_i)^2}{(n_j + n_i)^2 + (k_j - k_i)^2} \quad T_i = \frac{(1 - R_i R_i')e^{-4\pi k_i L_i/\lambda}}{1 - R_i R_i' e^{-8\pi k_i L_i/\lambda}}$$

where L is the length of the ith element, and λ the wavelength of incident light (μm). Based on Otanicar et al. [44], graphite and silver nanofluids' optical properties can be obtained. Also, T_1 and R_1 are 1.0 and 0.035, respectively. Those values can be used for obtaining the reflection of graphite and silver nanofluids (0.0365). Therefore, the reflectance of the nanfluids is approximately 3.65%. Since the reflection of pure water is 0.0366 (3.66%), the reflectance of aqueous nanofluids does not change significantly.

The thermal loss of the insulated sample with rubber pipe type insulation, as shown in Fig. A2, can be calculated by conduction heat transfer, using the thermal conductivity (0.13 W m^{-1} K^{-1}) and thickness (38mm) [23].

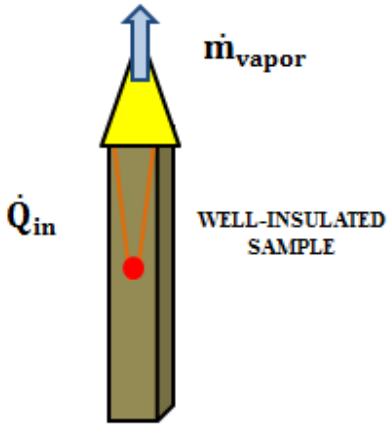

Figure A2. Well-Insulated Test Sample to Decrease Thermal Losses

$$Q = kA\frac{dT}{dx}$$

where Q is the heat transfer rate, k the thermal conductivity, A the area, and dT/dx the temperature gradient in x direction. Using this equation with those values, the result indicates that the thermal loss from the test sample is approximately 1%.

APPENDIX B

UNCERTAINTY CALCULATION FOR THE EXPERIMENTAL RESULS

The uncertainty of a measurement indicates its quality of experiments. It is important to distinguish between error and uncertainty. The error is the difference between the measured value and the true value, but the uncertainty is a quantification of the doubt about the measurement results [24]. The uncertainty comes from the measuring instrument, the stability of the item, the measurement process, operator skill, and the experimental environment [24]. Therefore, in order to reduce the uncertainty of the measurements, the calibration of the instrument should be done before conducting the experiments.

To simplify the calculations of the propagating uncertainty for h_{fg} experiments, the relative uncertainty should be employed. In order to find h_{fg}, the heat input (Q_{in}) is divided by the vapor mass generation (m_{vapor}). Therefore, the propagating uncertainty in h_{fg} can be found from the fractional uncertainties in the heat input (Q_{in} with uncertainty $u(Q_{in})$) and vapor mass generation (m_{vapor} with uncertainty $u(m_{vapor})$), Then, the relative uncertainty $u(h_{fg})/ h_{fg}$ is described as:

$$\frac{u(h_{fg})}{h_{fg}} = \sqrt{\left(\frac{u(Q_{in})}{Q_{in}}\right)^2 + \left(\frac{u(m_{vapor})}{m_{vapor}}\right)^2}$$

where u is the standard uncertainty. It is calculated from $u = \frac{s}{\sqrt{n}}$ (s is the standard deviation, and n the number of measurements).

For pure water, graphite nanofluids, and silver nanofluids experiments, based on instrument calibrations, the propagating uncertainty is calculated by the values of the heat input, the heat input uncertainty, the vapor mass generation, and the vapor mass generation uncertainty. As a result with five trials, for the laser-based experiments the relative

uncertainties are 13.5% for pure water, 15.6% for graphite nanofluid, and 15.4% for silver nanofluid. For comparison, the uncertainties of the laser-based experiments were calculated in [10] to be about 15% based on a level of confidence of 95%.